Numerical study of the static and pitching RISØ-B1-18 airfoil

Bertagnolio, Franck

Publication date:
2004

Document Version
Publisher's PDF, also known as Version of record

Risø–R–1448(EN)

Numerical Study of the Static and Pitching RISØ-B1-18 Airfoil

Franck Bertagnolio

Risø National Laboratory, Roskilde, Denmark
January 2004

Abstract The objective of this report is the better understanding of the physics of the aeroelastic motion of wind turbine blades in order to improve the numerical models used for their design. In this study, the case of the RISØ-B1-18 airfoil which was equipped and measured in an open jet wind tunnel is studied. Two and three-dimensional Navier-Stokes calculations using the $k-\omega$ SST and Detached Eddy Simulation turbulence models are conducted. An engineering semi-empirical dynamic stall model is also used for performing calculations. Computational results are compared to the experimental results that are available both for the static airfoil and in the case of pitching motions. It is shown that the Navier-Stokes simulations can reproduced the main characteristic features of the flow. The DES model seems also to be able to reproduce some details of the unsteady aerodynamics. The Navier-Stokes computations can then be used to improve the performance of the engineering model.

ISBN 87–550–3298–2 (Internet)
ISSN 0106–2840

Print: Pitney Bowes Management Services Denmark A/S · 2004

Contents

1 Introduction

The aim of this work is the better understanding of the physics of the aeroelastic motion of wind turbine blades in order to improve the numerical simulation of such dynamical systems. In previous works, both aerodynamic damping calculations and fully-coupled aeroelastic simulations of wind turbine blades were performed by using the CFD code EllipSys3D as a fluid flow model, and the aeroelastic code HAWC as a structural model [1, 2]. The results were compared with semi-empirical dynamic stall engineering models, such as the Beddoes-Leishman model [3]. However, the lack of experimental results in such configurations made it difficult to conclude which model was performing better. In order to clarify this issue, it was decided to come back to more basic cases for which experimental results exist in the litterature. Not many experimental campaigns exist for which the operational conditions (including Reynolds number, Mach number, etc...) are close to our concern, namely wind turbine applications. One of the rare experimental set-ups that meets these requirements is the measurements performed by Risø in the VELUX wind tunnel [4]. The airfoil profile that has been chosen for our comparative tests is the RISØ-B1-18 airfoil designed by Fuglsang *et al* [5].

The so-called Direct Numerical Simulation of the fluid flow dynamics (for which all the scales of the turbulent flow are simulated by the numerical code) around a turbine blade is still far out of reach of modern computers. Therefore, turbulence models have to be implemented in the numerical codes in order to reduce the computational costs to an acceptable size. Two types of turbulence modelling, which have been implemented in the Navier-Stokes code EllipSys3D, are considered in this paper. In a first place, the so-called Reynolds Averaged Navier-Stokes (RANS) approach using the $k-\omega$ SST turbulence model by Menter [6] has been implemented. The simulation of a wind turbine rotor with this model has proven to give sensible results [7] compared to the well-detailed measurements obtained during the NREL Unsteady Aerodynamics Experiment Phase VI performed by NREL at the NASA-Ames wind tunnel [8]. However, a more detailed study showed that the RANS approach alone was unable to correctly simulate the three-dimensional patterns in the flowfield around the 2D section of a pitching airfoil [9]. Conversely, the so-called Detached Eddy Simulation (DES) [10], which is a combination of a RANS approach in the vicinity of the blade and a Large Eddy Simulation (LES) in the far field, gave promising results [9]. Finally, two-dimensional simulations using the $k-\omega$ SST model will be performed, mainly due to their low computational costs, and in order to evaluate the discrepancies that can be expected with such simulations compared to three-dimensional and experimental results.

The ultimate goal of this work is to gain enough confidence in our Navier-Stokes solver so that it can be used as a tool for wind turbine airfoil design. However, the computational costs of 3D calculations are still prohibitive for realistic daily engineering applications. Our strategy is actually to use this detailed model in order to improve and tune already existing engineering models, which are currently used in the design processes for modelling aerodynamic forces exerted on wind turbine blades. The only model of this type that will be considered in this work is the dynamic stall model by Beddoes-Leishman [3].

The text is organised as follows. After presenting our numerical models and the experimental set-up, a preliminary study where several cases of a pitching airfoil are computed with our two-dimensional Navier-Stokes solver is performed. The numerical parameters (grid refinement, time step, etc...) for these computations are chosen on the basis of our previous experiences of such configurations, and may therefore not be optimal. Results are compared to experimental measure-

ments. The discrepancies are highlighted and will direct the following study which goal is to better understand the origin of such discrepancies, and improve our numerical models. A grid and time-step dependency analysis is performed with two-dimensional simulations, as three-dimensional computations are far too expensive to perform such a study. Therefore, the conclusions of this study will have to be extrapolated to the subsequent three-dimensional computations, being aware that three-dimensional effects were not included in the previous refinement analysis. The next step is the computation of a static airfoil at specific angles of attack in order to validate our Navier-Stokes solver in this more simple configuration. Thereafter, the case of a pitching airfoil is studied. The mean angle of attack will be chosen in the stalled range, as it was observed that the discrepancies were larger for the 2D simulations in this case. The next step is the validation and tuning of the engineering semi-empirical dynamic stall model. It will be shown how some parameters of the model can be modified in order to improve its results. Finally, the previous computational and experimental results obtained for the pitching airfoil are processed in order to compute the aerodynamic work exerted on the airfoil.

2 Numerical Models and Experimental Data

In this section, the different numerical models that are used at Risø for aeroelastic simulations are presented. The main focus of this work is the study of so-called Computational Fluid Dynamics (CFD) codes that solve the full Navier-Stokes equations for a fluid flow. The second class of models that are more often used by engineers for designing wind turbine airfoils, due to their computational efficiency, are the so-called semi-empirical dynamic stall models. In addition, the experimental facilities and measurements that will be refered to in this study to validate and compare our numerical models are described.

2.1 Navier-Stokes Solver

The fluid flow solver EllipSys3D, and its two-dimensional version EllipSys2D, were used for this study. This in-house code was developed in a co-operation between the Department of Mechanical Engineering at DTU (Technical University of Denmark) and the Department of Wind Energy at Risø National Laboratory. A detailed description of the numerical code can be found in the references [11, 12, 13].

It is designed to solve both the two-dimensional and three-dimensional Navier-Stokes equations for an incompressible fluid. It uses a cell-centered grid arrangement for the pressure field and the cartesian velocity components. The equations are discretised by means of a finite volume formulation. The well-known velocity-pressure decoupling is circumvented by using the Rhie and Chow interpolation technique [14]. For unsteady computations, the PISO algorithm is used for solving the momentum and pressure equations in a predictor-corrector fashion [15]. The Second order Upwind Differencing Scheme (SUDS) is applied to compute the convective fluxes [16], whereas viscous terms are discretised with the classical second order central difference scheme. A subiteration technique is implemented in order to increase the critical time step.

In order to model turbulence, a model must be implemented in the fluid flow solver. In our case, the $k-\omega$ SST turbulence model by Menter [6] in its original version was used to obtain the turbulent viscosity. In the case of three-dimensional simulations, a Detached Eddy Simulation (DES) technique was also implemented [17]. This model uses the above mentioned $k-\omega$ SST model in the vicinity of the airfoil, avoiding the need for highly refined grid cells in this region of the flow, whereas a Large Eddy Simulation (LES) model, namely a Smagorinsky-like model [18], is used in the far field. LES models fully simulate the unsteady dynamics of the larger scales of the flow, whereas the smaller eddies which cannot be captured by the computational grid (also refered to as subgrid scales) are modelled by an algebraic turbulent eddy viscosity class model.

It is emphasized that in all our computations, the flow was assumed to be fully turbulent and no transition model was implemented.

The numerical code requires that the computational domain must be mapped onto a boundary-fitted structured grid. In order to facilitate the mapping and to take advantage of the new generation of parallel computers, a domain decomposition technique has been implemented in the numerical code. The meshes of the individual subdomains must be conformal, i.e. the grid lines must match at the interfaces between the subdomains. In a parallel computing platform, each processor is handling a certain number of subdomains. The communications between the several processors are performed by using the MPI-library.

2.2 Dynamic Stall Model

In this study, only one engineering semi-empirical dynamic stall model was tested: the Beddoes-Leishman model [3]. This model uses as an input the static lift, drag and moment characteristics as a function of the angle of attack. Based on these data, and by adjusting a certain number of modelling parameters, the model is able to predict the aerodynamic forces, namely lift and drag, and moment, exerted by the fluid flow on the airfoil during the dynamic motion of the airfoil, such as a plunge, lead-lag or pitching motion. In this study, only the case of a pitching airfoil will be studied.

Note that the original Beddoes-Leishman model was slightly modified for our particular purpose [19]. In particular our implementation does not include leading edge separation, and the effects of dynamic moment were ignored.

2.3 Wind Tunnel Tests of the RISØ-B1-18 Airfoil

The VELUX wind tunnel is an open jet test section which has a cross section of $7.5 \times 7.5\,m$ and a length of $10.5\,m$. The cross section of the quadratic jet blowing into the test section is $3.4 \times 3.4\,m$. The maximum flow velocity is $42\,m/s$. It has a background turbulence intensity of 1%. A more complete description of the wind tunnel and the test stand for 2D airfoil sections can be found in Fuglsang *et al* [4].

The RISØ-B1-18 airfoil was equipped and measured in the VELUX wind tunnel by Fuglsang *et al* [5]. The airfoil section had a chord $C = 0.6\,m$, the inlet flow velocity was set to $V_\infty = 42\,m/s$, resulting in a Reynolds number equal to 1.6×10^6. The two-dimensional airfoil span was $1.9\,m$ and end plates were used at each extremity to minimize 3D flow effects. Measurements comprised both static and dynamic inflow. Dynamic inflow was obtained by pitching the airfoil in a harmonic motion around an axis located at 40% of the chord (starting from the leading edge) resulting in a harmonic variation of the angle of attack. The reduced frequency of the periodic motion was:

$$k = \frac{\omega C}{2V_\infty} = 0.09$$

where ω is the angular velocity. The amplitude of the pitching motion was $A = \pm 2^o$, with small variations from one test case to the other due to experimental conditions.

In this work, we will mainly refer to the pitching motion measurements performed for a mean angle of attack of $\alpha_m = 15.9^o$ and an amplitude of $A = 2.2^o$. However, a preliminary study and a mesh refinement study will also be using the static measurements and several pitching configurations.

Note that all results that will be displayed in the figures in this report involve dimensionless quantities (except for angles of attack that will be measured in degrees). The reference quantities used for non-dimensionalisation will always be the airfoil chord length, the inflow velocity, and the air density and viscosity.

3 Preliminary Study

As a starting point for our study, two-dimensional simulations of the flow around the RISØ-B1-18 airfoil were performed with the Navier-Stokes solver EllipSys2D. A 2D mesh, which will be refered to in the following as the preliminary grid, was generated as follows. It is an O-mesh involving 256 cells around the airfoil and 128 cells away from the airfoil. The outer boundary is located at 20 chords away from the airfoil. The height of the first grid cell (non-dimensionalised by the chord length) is equal to 1×10^{-5}. This configuration was chosen as this kind of grid has proven to be refined enough in most of the numerical test cases performed in previous studies (see [20] for example).

3.1 Static Airfoil

Firstly, steady state computations were performed for various angles of attack varying from 0 to 24^o. The computed lift and drag are compared with averaged experimental measurements on Figures 1(a-b). It can be seen that the lift is very well predicted by our numerical model, whereas the computed drag is slightly lower before stall and higher after stall compared to experimental results. However, these discrepancies remain relatively small.

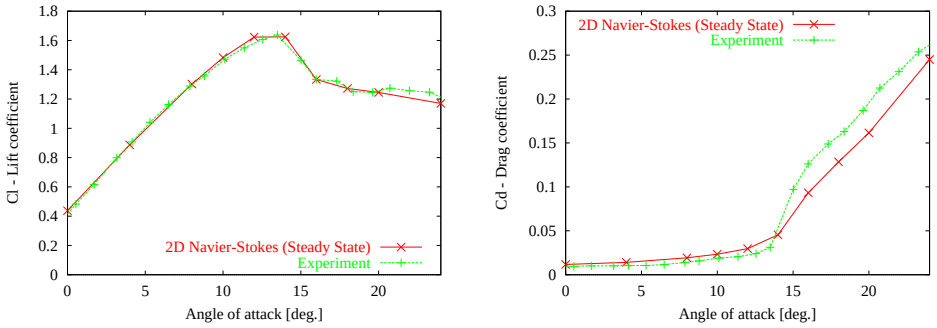

(a) Lift (b) Drag

Figure 1. Polar Characteristics

3.2 Pitching Airfoil

Secondly, the cases of a pitching airfoil at several mean angles of attack were studied. The configurations correspond to the experimental cases as described in Fuglsang *et al* [5]. Naturally, the computations were unsteady and the time step was set to $\Delta t = 1 \times 10^{-3}$ (non-dimensionalised by the airfoil chord length and the inlet velocity). The computed lift and drag loops as a function of the angle of attack are compared with experimental results on Figs.2 and 3. The results obtained with the Beddoes-Leishman model are also reported. Note that the latter model has been fitted as an input with the steady state data originating from the lift and drag coefficients computed with the Navier-Stokes solver as mentioned above.

It can be observed that the lift loops are in relative good agreement before stall occurs, i.e. up to $\alpha_m = 11^o$, although the opening of the loops obtained with the Beddoes-Leishman model is smaller. Conversely, for mean angles of attack equal and larger than 15.9^o, the loops start to differ in shape, opening and slope. The loops from Beddoes-Leishman model have a tendency to follow the shape of the polar characteristic curve.

As for the drag, larger discrepancies can be observed. Before stall, the drag loops have quite different openings. Moreover, and as it could be expected from the previous static airfoil computations, there exist quite big differences in the average levels of drag after stall, namely the computed drag is smaller than the experimental one. Finally, the opening of the loops becomes very small for the Beddoes-Leishman model.

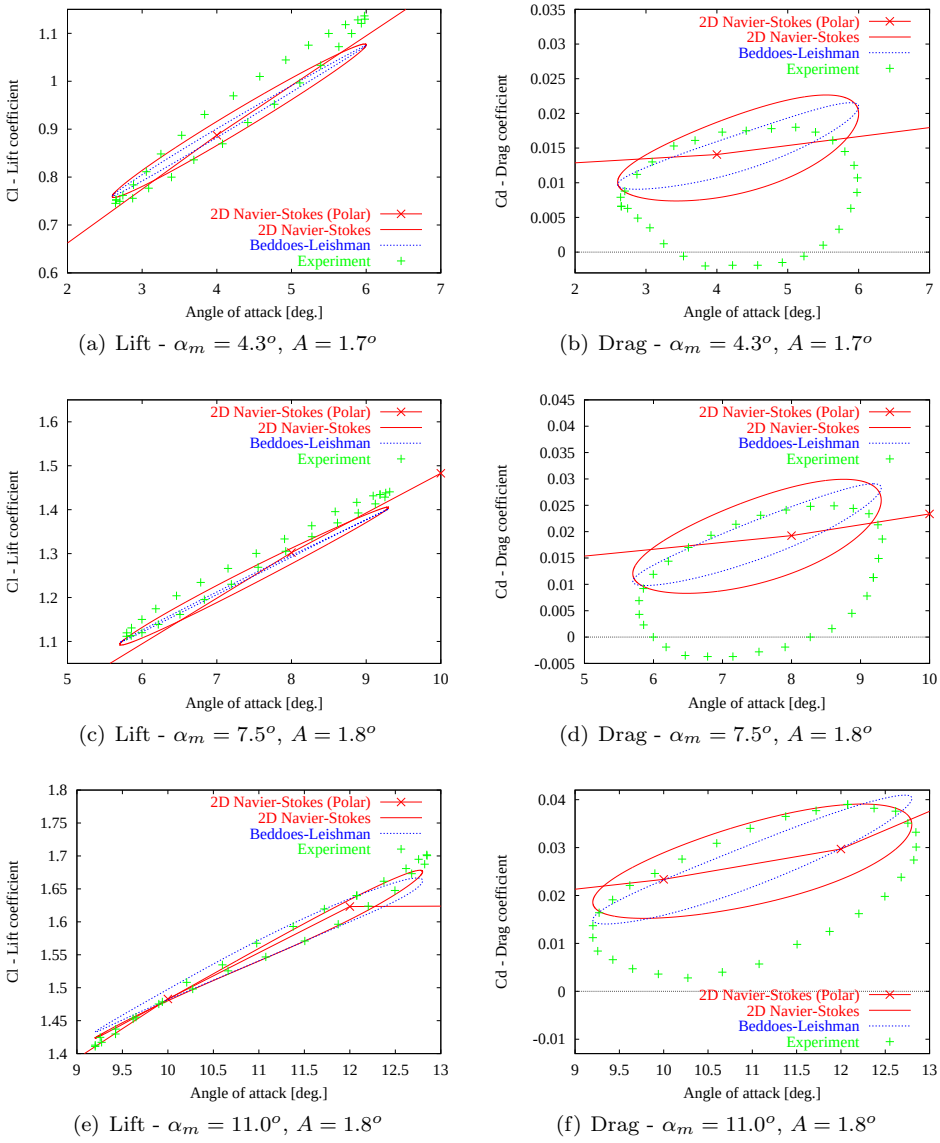

(a) Lift - $\alpha_m = 4.3^o$, $A = 1.7^o$

(b) Drag - $\alpha_m = 4.3^o$, $A = 1.7^o$

(c) Lift - $\alpha_m = 7.5^o$, $A = 1.8^o$

(d) Drag - $\alpha_m = 7.5^o$, $A = 1.8^o$

(e) Lift - $\alpha_m = 11.0^o$, $A = 1.8^o$

(f) Drag - $\alpha_m = 11.0^o$, $A = 1.8^o$

Figure 2. Characteristic Loops for Pitching Airfoil

3.3 Conclusions

As a conclusion, if the experimental results can be taken as a reference (which is in itself questionable as the measurement data involve uncertainties and also numerous corrections due to the experimental set-up, see [4]), it is quite difficult to conclude which of the Navier-Stokes solver or the Beddoes-Leishman model is performing better. This motivates the remainder of this paper, namely a closer study of the numerical simulation of a static and pitching airfoil.

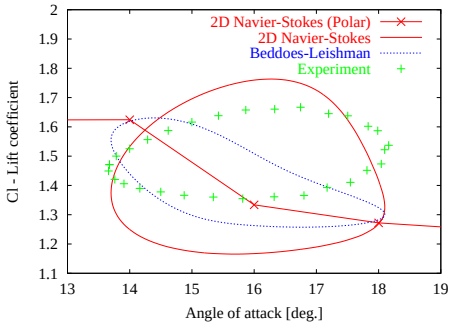

(a) Lift - $\alpha_m = 15.9^o$, $A = 2.2^o$

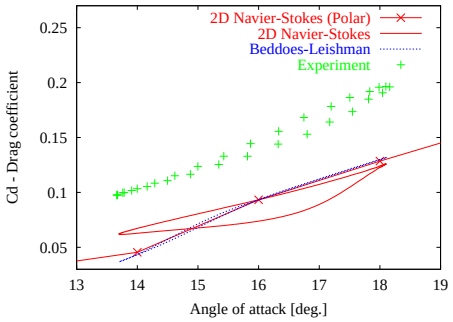

(b) Drag - $\alpha_m = 15.9^o$, $A = 2.2^o$

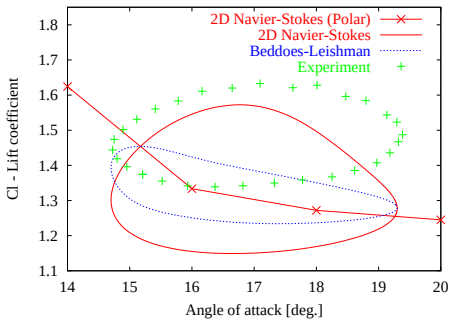

(c) Lift - $\alpha_m = 17.0^o$, $A = 2.3^o$

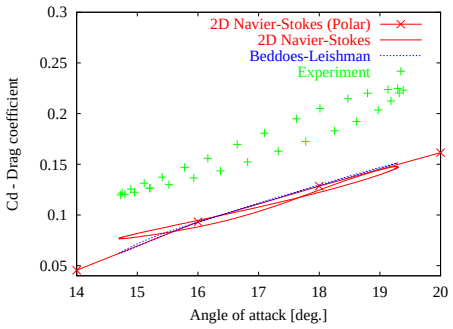

(d) Drag - $\alpha_m = 17.0^o$, $A = 2.3^o$

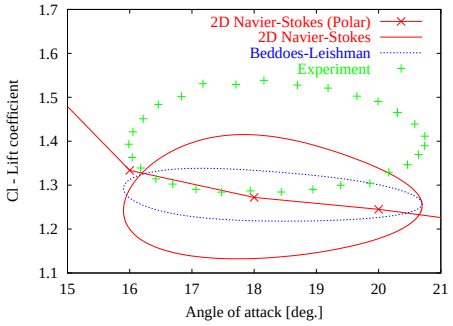

(e) Lift - $\alpha_m = 18.3^o$, $A = 2.4^o$

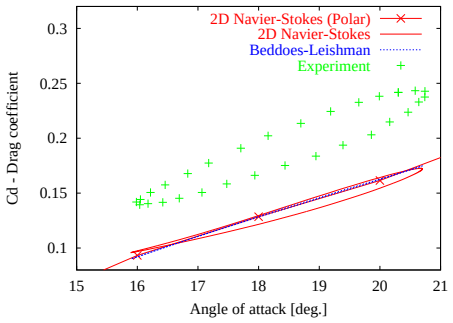

(f) Drag - $\alpha_m = 18.3^o$, $A = 2.4^o$

Figure 3. Characteristic Loops for Pitching Airfoil (continued)

4 Grid and Time-Step Dependency Analysis

Due to the high computational costs of three-dimensional computations, this study is performed with the two-dimensional version of the Navier-Stokes solver Ellip-Sys2D. It is therefore expected that it is not fully relevant for the three-dimensional dynamics of the fluid flow around the airfoil section that will be studied in the remainder of this work. However, a grid which is already too coarse for a 2D computation is obviously unsuitable for 3D computations. Therefore, this study can give some indications on the refinement requirements when performing 3D computations.

4.1 Grid Refinement

All the grids tested have the following characteristics. These are O-type mesh extending to 20 chord lengths from the airfoil. The grid generation is such that the cells are roughly square from 1/10 of the chord length away from the airfoil up to one chord length (see pictures of the reference grid defined below in Fig.4). This last particular feature is required for the DES computations that will be performed in the following of this study. Indeed, the use of a LES model in the far field requires that the cells are square in order to improve its accuracy.

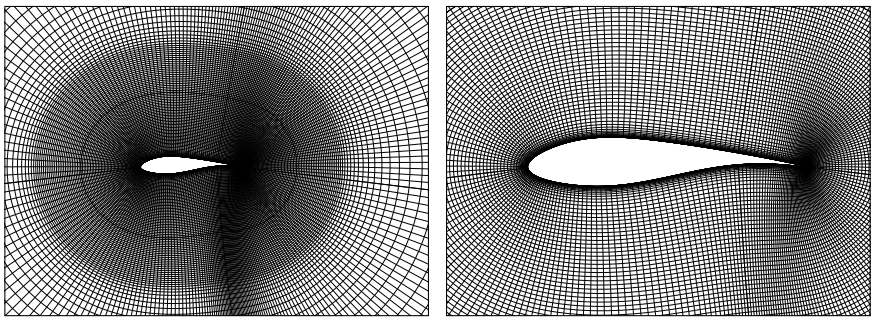

(a) Extended View (b) Detailed View

Figure 4. Reference Grid

Our reference grid involves 256 cells on the airfoil and 128 away from the airfoil. The height of the first cell on the airfoil is 1×10^{-5} (non-dimensionalised with respect to the chord length). The grid is stretched toward both the trailing and the leading edge of the airfoil (Fig.4).

In order to check that the grid generation strategy (involving the definition of square cells in the neighbourhood of the profile) does not influence too much the results of our preliminary study, the polar characteristics obtained with the present reference grid are compared to those of the original preliminary grid of the previous section. Both computations were performed as steady state. As it can be seen on Fig.5, the main difference is that the computed lift from the reference grid is slightly overpredicted after stall.

Our refinement study strategy consists in two steps. The reference grid was first refined in the direction along the airfoil, then in the direction away from the airfoil. All results presented in this refinement study are obtained from steady state computations.

Refinement of the Mesh Along the Airfoil

In the first step, three grids are defined in addition to the reference grid. The

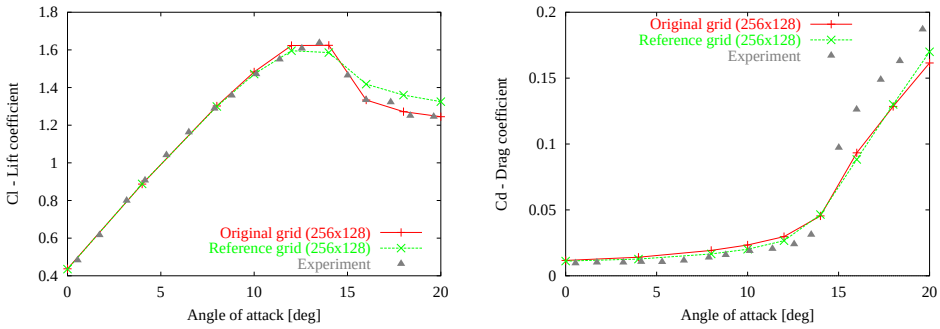

(a) Lift (b) Drag

Figure 5. Polar Characteristics - Comparison of Original and Reference Grids

first grid is obtained by doubling the number of cells around the airfoil (i.e. 512 cells). The second one involves 768 cells. Finally, as it is believed that more points are needed on the suction side of the airfoil when performing three-dimensional unsteady computations in order to better capture the dynamics of the detached unsteady vortices, a third mesh involving the same number of cells as the reference mesh, was created by removing some points from the pressure side and adding them to the suction side. This last one will be refered to as 'i-adapted mesh 256x128'.

Lift and drag coefficients as a function of angle of attack are reported on Figs.6(a-b). As it can be seen, there are few differences between the different meshes. The two refined meshes give very similar results, whereas the reference mesh and the i-adapted mesh give very close results as well. The small discrepancies are only noticeable at high angles of attack.

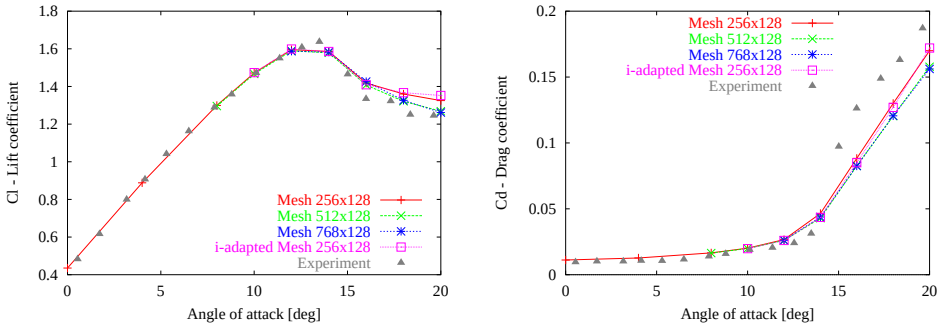

(a) Lift (b) Drag

Figure 6. Polar Characteristics - Mesh Refinement in i-Direction

Refinement of the Mesh Away from the Airfoil

In the second step, four additional meshes are defined in addition to the reference one. The two first meshes are defined by increasing the cell numbers away from the airfoil, respectively to 256 and 384. The extend of the region for which the cells are maintained roughly square is kept constant, so that the two meshes point distributions remain similar and can be compared. In other words, the heights of the first cell and of the cells in the above mentioned region decrease as the total number of cells increases. A third and fourth mesh are defined by removing some points in the far field (where it is believed that the dynamics of the vortices is not so important for the characteristics of the airfoil) and adding them in the vicinity of the airfoil. They respectively involve 128 and 384 cells away from the airfoil. They are respectively named 'j-adapted mesh 256x128' and 'j-adapted mesh

256x384'.

The results are reported on Figs.7(a-b). It can be seen that the lift and drag are sensitive to the mesh refinement in, and particularly after, the stall region. Lift noticeably increases in the post-stall region when the mesh is refined. The j-adapted mesh 256x128 is performing slightly better (i.e. results closer to those of the refined meshes) in the stall region than the reference mesh, but similar results as the reference mesh are recovered in the post-stall region. Contrarily to the j-adapted 256x128 grid, the j-adapted 256x384 grid does not modify the results in the stall region, compared to the corresponding refined 256x384 mesh. Therefore, it is considered that both these finest grids give converged results. The intermediate refined grid containing 256x256 cells exhibits results intermediate between the coarser grids (reference and j-adapted grid 256x128) and the finer grids (256x384 mesh and j-adapted 256x384 mesh), and these are actually a bit closer to those of the finest grids.

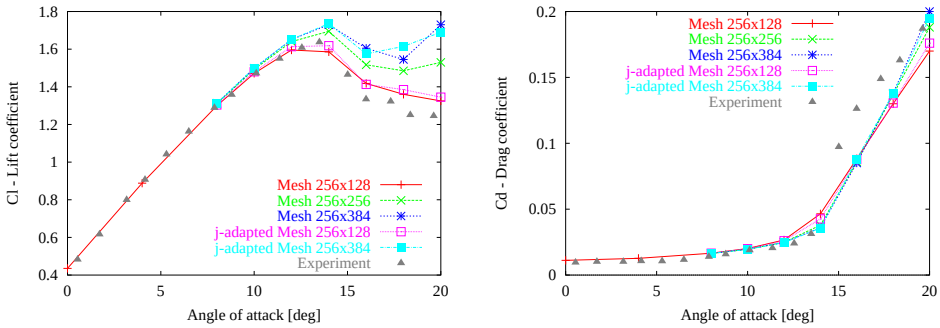

(a) Lift (b) Drag

Figure 7. Polar Characteristics - Mesh Refinement in j-Direction

4.2 Choice of the Final Grid

In view of the previous results, a combination of the i-adapted 256x128 grid and the grid containing 256 cells away from the airfoil is created. It then contains 256x256 cells. The reasons for this choice are as follows. The i-adapted grid configuration was chosen in order to increase the number of cells on the suction side of the airfoil where most of the dynamics relevant for the airfoil characteristics is supposed to take place.

Even if the previous results proved that the grid containing 256 points away from the airfoil didn't exhibit quite converged results (compared to the grid even finer in this direction), this configuration was nevertheless chosen for computational cost reasons. Indeed, the three-dimensional DES computations that will be performed in the following are very time-consuming and a more refined mesh would require far too long computational times. However, the quality of the results obtained with the grid containing 256 points were considered as satisfactory regarding the small improvements that can be obtained by increasing the number of cells (see results of grid involving 384 points away from the airfoil). This also implies that the height of the first cell on the airfoil is 5×10^{-6}.

This grid, which will be refered to as the final grid, will be used for all 2D computations in the remainder of this work.

4.3 Time-Step Analysis

The influence of time step is studied by performing both steady state and unsteady computations using the above described final grid. As it can be seen on Figs.8(a-b), reducing the time-step from $\Delta t = 2\times10^{-2}$ to 5×10^{-3} (non-dimensionalised by the chord length and the inflow velocity) does not significanlty change the computational results, except for the lift at high angles of attack. By reducing the time-step, the lift curve converges toward the steady state results. However, it can be seen that unsteady computations predict higher lift at high angles of attack compared to the steady state computations, which already predict too high lift compared to the experimental results after stall. Very small discrepancies between the different Navier-Stokes computations can be observed on the drag coefficient.

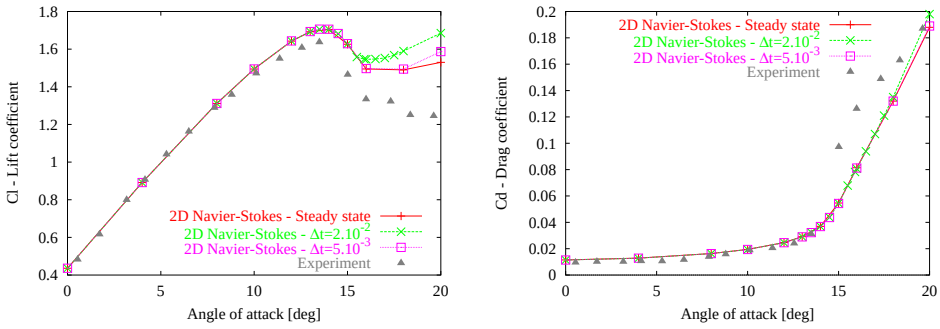

(a) Lift (b) Drag

Figure 8. Polar Characteristics - Final Grid - Time Dependency Analysis

In the remainder of this work, all computational results that will be presented originate from unsteady computations, and the time step will always be set equal to $\Delta t = 2\times10^{-2}$.

4.4 Grid Generation for 3D Computations

The grid used for all 3D computations in this study (unless otherwise specified) is based on the final grid that just has been defined above for the 2D computations. It is simply generated by lining up the same 2D grid in the spanwise direction. The cell size in the spanwise direction, i.e. the distance between 2 identical two-dimensional grids next to each other along the airfoil span, is equal to 2×10^{-2}, and there are 128 cells in that direction. Consequently, the total mesh extends over a length of 2.56 airfoil chords in the spanwise direction. Periodic boundary conditions are enforced at the two extremities of the blade section. Even if this configuration is not fully identical to the actual experiment (for which there exist solid walls at each end of the airfoil section to prevent the occurence of three-dimensional effects), one may hope that the middle section of the experimental setup where the measurements are performed will be free of the influence of the walls, and therefore computational and experimental results can be compared.

5 Static RISØ-B1-18 Airfoil

The objective of this section is firstly to validate our Navier-Stokes solver for the computation of a static airfoil. Secondly, as the case of a pitching airfoil will be studied in the following, it is important to evaluate how far the flow field for the static airfoil computed by our numerical model deviates from experimental results. It will thereby provide a basis for our comparisons when simulating the pitching motion in the following.

5.1 Description of the Test Case and Numerical Computations

The experimental results that are available for this configuration are quasi-steady measurements. They were performed by continuously varying the angle of attack, slowly enough so that the inflow velocity can be considered as steady for each measurement step [5].

Both 2D and 3D Navier-Stokes computations were conducted. In both cases, the simulations are unsteady computations and the time step was always set equal to $\Delta t = 2 \times 10^{-2}$ (non-dimensionalised by chord length and inflow velocity).

The 2D computations make use of the final grid described in section 4.2, and of the $k-\omega$ SST turbulence model. The angles of attack that are considered range from 0^o to 24^o.

As for the 3D computations, the 3D grid generated from the previous 2D final grid as described in section 4.4 was used. As the pitching airfoil configuration for a mean angle of attack $\alpha_m = 15.9^o$ will be studied into details in the following of this study, we will concentrate on angles of attack within this region (scanning the whole range of angles of attack being too expensive for 3D computations). Moreover, the angle of attack for which stall occurs for our 3D Navier-Stokes model will be evaluated. The DES technique (which is supposed to be the most accurate turbulence model at our disposal) will be used for most of the computations. Five angles of attack are considered: $\alpha = 10^o, 12^o, 13^o, 13.5^o$ and 15.9^o. In the experiment, these angles scan the region in which stall occurs. Nevertheless, the $k-\omega$ SST model will also be used for a single angle of attack $\alpha = 15.9^o$ in order to evaluate the influence of the three-dimensional effects compared to 2D simulations with the same turbulence model.

5.2 Analysis of the Results

2D $k-\omega$ SST and 3D DES Computations

Polar Characteristics

As it can be seen on Figs.9(a-b), the 2D Navier-Stokes model overpredicts the lift and underpredicts the drag after stall compared to the experimental results. Stall is predicted approximately at the same angle of attack as in the experiment. There is a good agreement before stall.

The 3D DES Navier-Stokes computations is matching almost perfectly the experimental results before stall ($\alpha = 10^o, 12^o$). However, stall is predicted slightly earlier (between 12^o and 13^o) than in the experiment, and the loss in lift and increase in drag due to stall are more abrupt. For the angle of attack $\alpha = 15.9^o$, the 3D DES results and the measurements are again in very good agreement.

It should be noted that these 3D DES computations were performed without transition modelling. However, it is well known that the implementation of a transition model has two important effects on Navier-Stokes computations. Firstly,

it increases the computed lift and decreases the drag, and secondly, it postpones the stall toward higher angles of attack. Therefore, it can be expected that a 3D DES computation with transition modelling would probably better capture the angle of attack for which stall occurs, at the expense of a too high computed lift and too low drag.

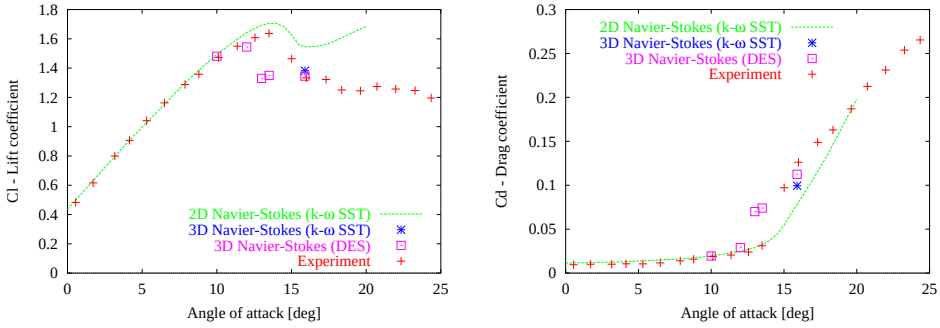

(a) Lift (b) Drag

Figure 9. Polar Characteristics for Static Airfoil

Times-Series and Spectrum Analysis

In order to have a closer look into the details of the flow, time-series of lift and drag are presented in Figs.10(a-b). The discrepancies in lift and drag levels between 2D and 3D DES computations are recovered. It can be noticed that the 3D DES computation is much less regular in time than the two-dimensional one, even if 2D results exhibit a periodic pattern. A Fast Fourier Transform (FFT) analysis of the signals shows that this periodic pattern is also present in the 3D flow, though at a slightly lower frequency (Figs.11(a-b)). It is identified as a vortex shedding from the trailing edge of the airfoil, as it will be shown more clearly in the following. However, visualisations of the computed 2D flow made this conclusion quite clear.

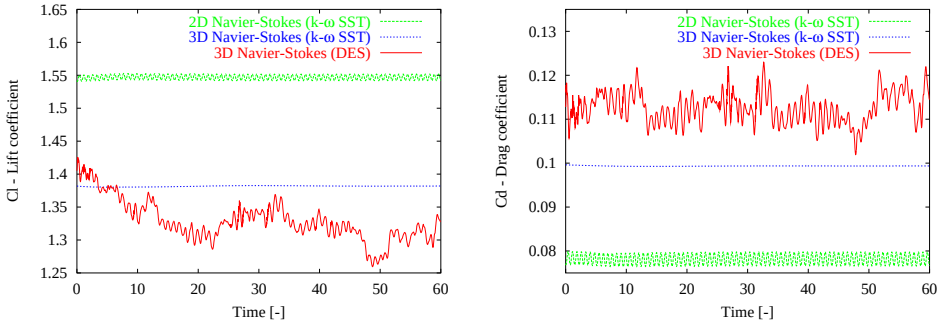

(a) Lift (b) Drag

Figure 10. Time-Series of Lift and Drag for Static Airfoil ($\alpha = 15.9^o$)

Spanwise Slices

The distribution of lift and drag along the airfoil in the spanwise direction for the 3D DES computation is studied next. Time-series of lift and drag at four specific stations along the airfoil are plotted on Figs.12(a-b). The FFT of these signals are reported on Figs.13(a-b).

It can be seen that the flow field clearly exhibits three-dimensional patterns. Indeed, Fig.12 shows that the lift and drag forces computed at the several stations exhibit long time scale oscillations (i.e. longer than a characteristic time period of 1, non-dimensionalised by the airfoil chord and the inlet velocity) which are

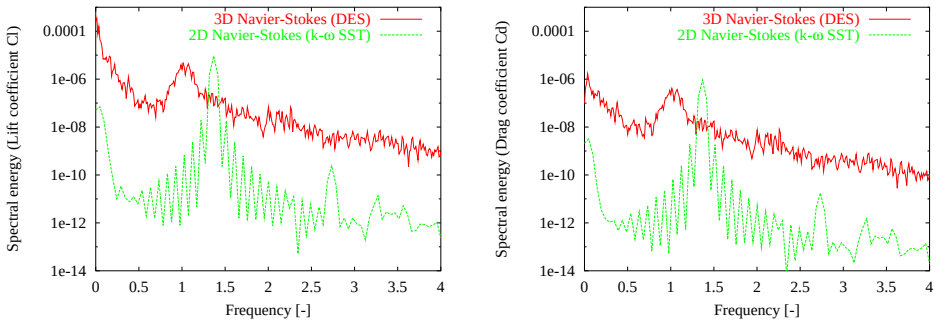

(a) Lift (b) Drag

Figure 11. Power Spectrum of Lift and Drag for Static Airfoil ($\alpha = 15.9^o$)

not correlated in time between the different stations. This clearly indicates the presence of vortex structures at some stations on the airfoil which are not present at other places. Therefore, they can be assimilated to 3D structures.

In addition, the FFT analysis shows that the 2D pattern observed on the lift and drag averaged over the whole airfoil span is present at all stations along the airfoil (see the spectral energy peaks for all curves at a frequency approximately equal to 1 on Fig.13) . Looking closely at these short time scale variations (i.e. of characteristic time period approximately equal to 1) of lift and drag on Fig.12, it is quite clear that these 2D patterns at all stations along the airfoil are quite well correlated in time. This indicates the presence of such a 2D vortex shedding phenomenon, on the top of the uncorrelated 3D structures along the airfoil span. Compared to the 2D results from Figs.10(a-b), these 3D patterns are then clearly responsible for the loss in averaged lift and increase in drag observed in the 3D DES computations.

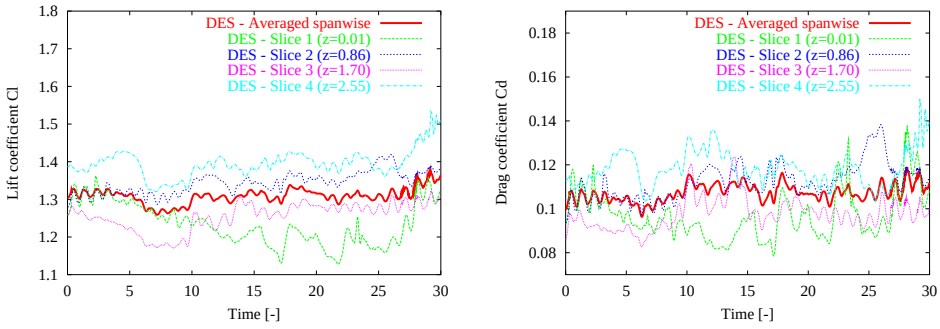

(a) Lift (b) Drag

Figure 12. Time-Series of Lift and Drag Spanwise along Static Airfoil ($\alpha = 15.9^o$)

Local Testing Points

To get a better idea of what is happening locally on the airfoil for the 3D DES computation, eight testing points are defined at the middle section of the airfoil located at the spanwise location $z = 1.14$. The testing point locations on the profile are displayed on Fig.14. Time-series of pressure and skin friction are reported on Figs.15 and 16 respectively, on the pressure and on the suction side. Results for the three last points on the suction side (points #6, #7 and #8) clearly show that the flow remains separated at all time on this part of the airfoil. Indeed, pressure and skin friction coefficient levels for these three points are significantly lower than for point #5, indicating the presence of the detachment point between point #5 and point #6, and a separated flow region downstream.

The respective FFTs corresponding to these signals are displayed on Figs.17

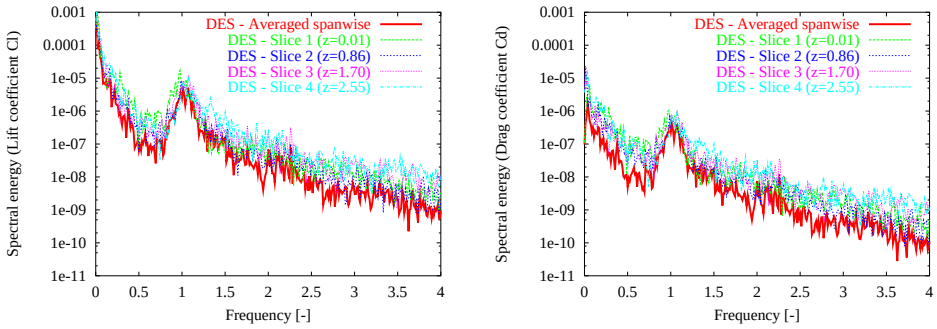

(a) Lift (b) Drag

Figure 13. Power Spectrum of Lift and Drag Spanwise along Static Airfoil ($\alpha = 15.9^o$)

and 18. The dimensionless characteristic frequency of 1 corresponding to the vortex shedding is clearly seen on all points except for the last three points (for the skin friction coefficient). It doesn't mean though that this frequency does not exist at these points. It is only because the signals at these points include a lot of other frequencies due to the highly turbulent nature of the flow in the detached region of the flow. Therefore, the characteristic frequency of the vortex shedding is hidden at these points by the presence of other vortices with characteristic frequencies close to 1.

A second conclusion that can be drawn from these results is the fact that the 2D vortex shedding has a global effect on the airfoil section - not only on the suction side where the phenomenon takes place, but also on the pressure side, since the peak at a characteristic frequency of 1 can be observed at all around the profile.

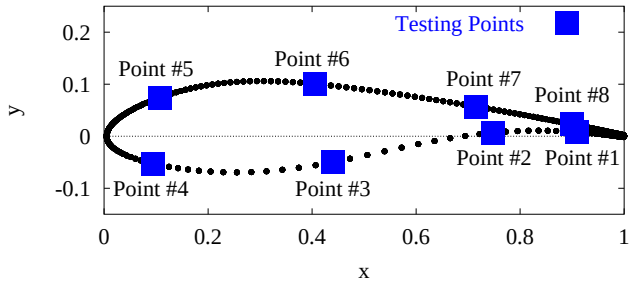

Figure 14. Testing Point Locations on the RISØ-B1-18 Profile

Comparison with Experimental Results

In order to assess if the 2D flow pattern observed in the previous computations (and identified as a trailing edge vortex shedding) also exists in reality, experimental results are analyzed. The characteristic frequency associated to this phenomenon is relatively high, and it was found that the measurements performed at a sampling frequence of $100Hz$ which were used above are not accurate enough. Therefore, a secondary measurement with a sampling frequence of $500Hz$ is now analysed. As described in section 5.1, during this measurement session the angle of attack was slowly increased, and lift and drag were measured. The angle of attack can then be considered as quasi-steady. The measurement data that are analysed in the following correspond to a variation of the angle of attack from 15^o to 21^o.

FFTs of the experimental lift and drag time histories are performed. Fig.19 displays the results for both lift and drag. As it can be seen, a clear pick can be

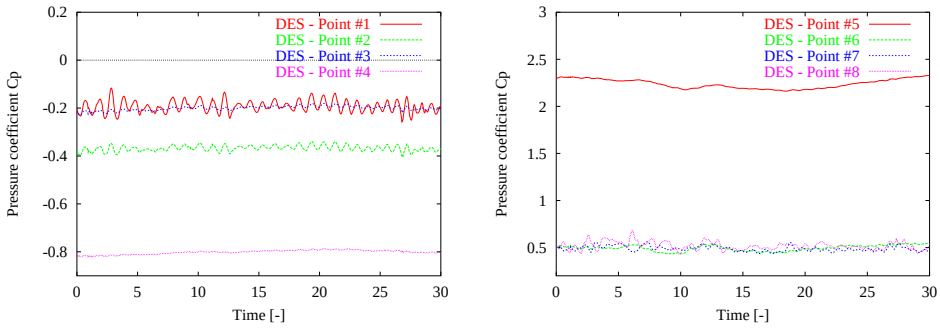

(a) Pressure Side (b) Suction Side

Figure 15. Time-Series of Pressure Coefficient at Middle Airfoil Section ($\alpha = 15.9^o$)

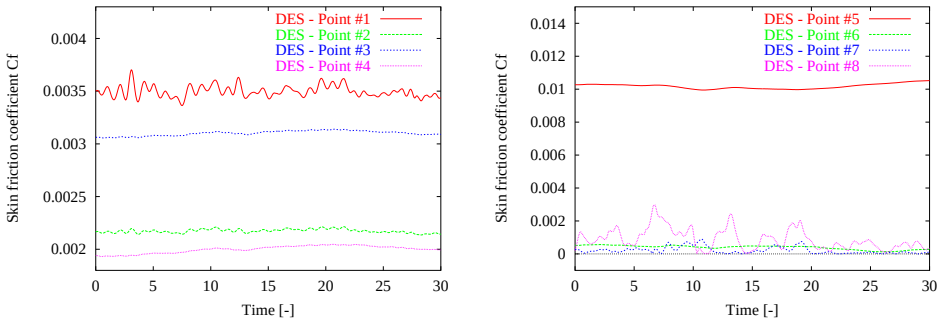

(a) Pressure Side (b) Suction Side

Figure 16. Time-Series of Skin Friction Coefficient at Middle Airfoil Section ($\alpha = 15.9^o$)

observed on the lift (at a dimensionless frequency approximately equal to 0.7). However, it does not clearly appear on the drag. These curves are to be compared with Figs.11(a-b) which display the same quantities for the 2D $k-\omega$ SST and the 3D DES computations, for which it was found that the 2D pattern characteristic frequency was present in both the lift and drag. Therefore, even if the characteristic frequency observed in the measurements is relatively close to 1 (i.e. the frequency observed in the computations), it remains questionable if this peak corresponds to the same 2D flow pattern.

3D $k-\omega$ SST Computation

In order to understand whether the good results obtained with the 3D DES computation at $\alpha = 15.9^o$ are due to the turbulence modelling or the capture of 3D features, an additional 3D computation with the $k-\omega$ SST turbulence model was performed. As if can be seen on both Figs.9(a-b), the 3D computation with the $k-\omega$ SST model recovers almost the same results as the 3D simulations with the DES model (compared to 2D results with the $k-\omega$ SST model).

Surprisingly, it can be seen on the time-series of lift and drag on Figs.10(a-b), that the 3D $k-\omega$ SST Navier-Stokes simulation predicts a steady flow (even if the computation uses an unsteady simulation technique). Fig.20 show the time-series of lift and drag at different spanwise locations along the airfoil section, as well as the averaged lift and drag along the airfoil. It can be seen that the force distribution is not uniform along the span of the airfoil, suggesting the fact that the flow field, even if steady, is not purely two-dimensional. This is confirmed by Fig.21 which displays the iso-pressure contours on the surface of the airfoil, and the iso-vorticity contours on two planes perpendicular to the main flow direction. It

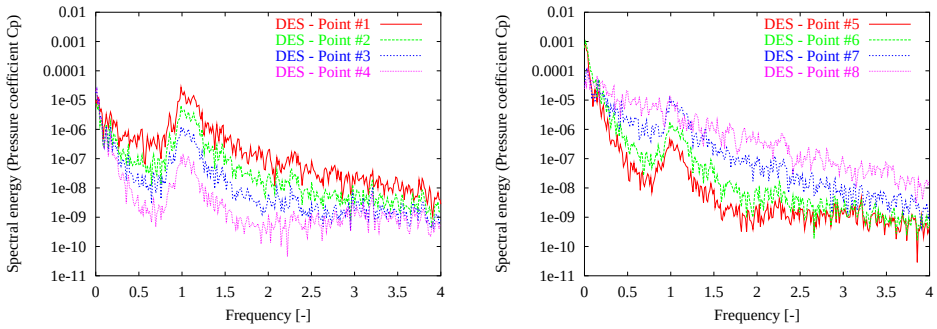

(a) Pressure Side (b) Suction Side

Figure 17. Power Spectrum of Pressure Coefficient at Middle Airfoil Section ($\alpha = 15.9^o$)

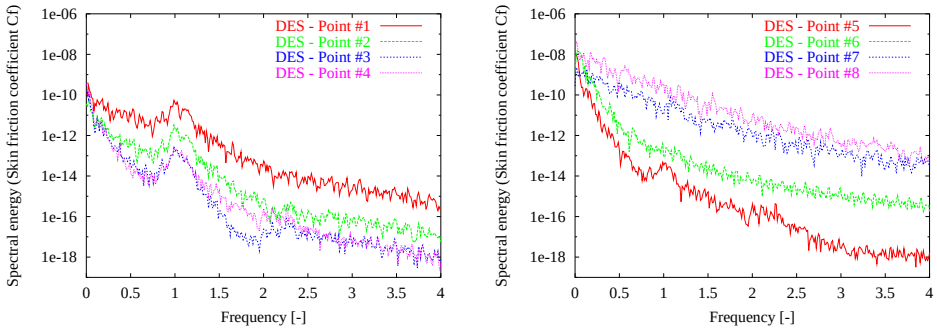

(a) Pressure Side (b) Suction Side

Figure 18. Power Spectrum of Skin Friction Coefficient at Middle Airfoil Section ($\alpha = 15.9^o$)

can clearly be seen that there exist two vortical structures indicating that the flow separation location is not constant along the spanwise direction, explaining the variation in drag and lift along the blade. This three-dimensional structure seems to be stable, at least numerically since no instability was generated during the time of the computation, which was carried out for a time of 200 (non-dimensionalised with respect to airfoil chord length and inflow velocity).

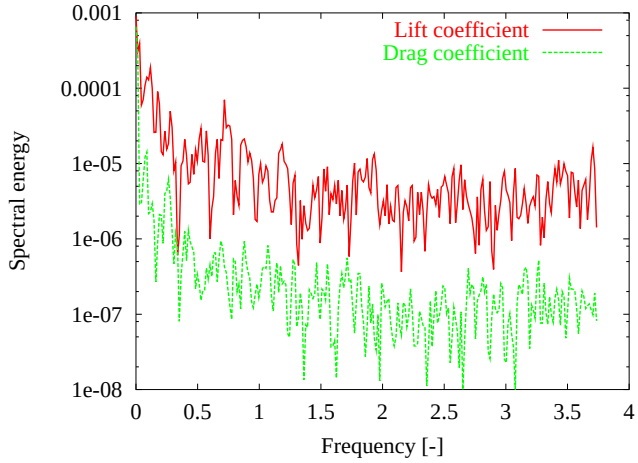

Figure 19. Power Spectrum of Lift and Drag for 500Hz Sampling Measurement

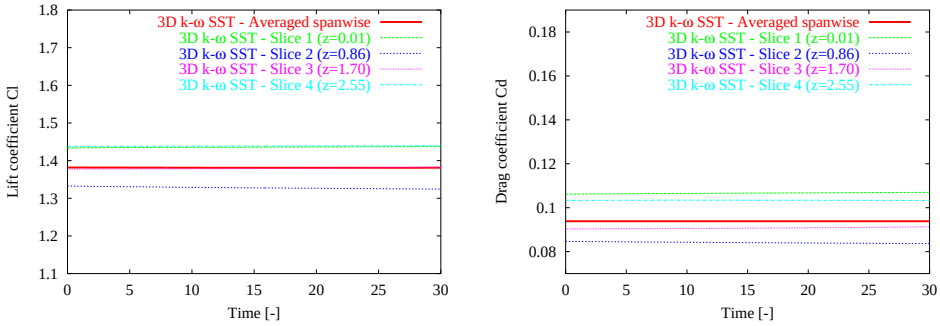

(a) Lift (b) Drag

Figure 20. Time-Series of Lift and Drag Spanwise along Static Airfoil ($\alpha = 15.9^o$)

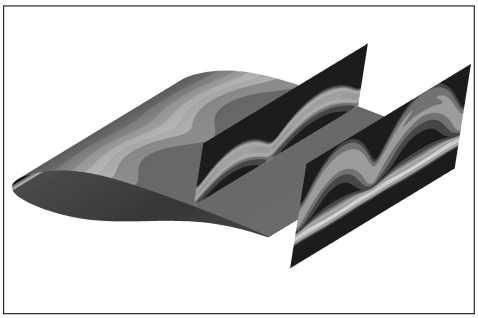

Figure 21. Details of Iso-Vorticity and Iso-Pressure for the Static Airfoil ($\alpha = 15.9^o$) - 3D $k-\omega$ SST

6 RISØ-B1-18 Airfoil in Pitching Motion

This section constitutes the core of this study, namely the numerical simulation, and comparison of the results with measurements, of a pitching airfoil.

6.1 Description of the Test Case and Numerical Computations

The test case considered corresponds to the experimental configuration for which the mean angle of attack is equal to $\alpha_m = 15.9^o$ and the pitching motion is a sinusoidal variation of the airfoil with an amplitude $A = 2.2^o$ [5]. The pitching motion is then described by the variation of the angle of attack as:

$$\alpha(t) = 15.9 + 2.2\sin(\omega t) \tag{1}$$

for which the angular velocity ω is related to the reduced frequency as:

$$k = \frac{\omega C}{2V_\infty} = 0.09 \tag{2}$$

where C is the airfoil chord, and V_∞ is the inlet velocity.

As in the previous section, when FFT analysis will be performed, the frequency will be non-dimensionalised by the airfoil chord and the inflow velocity.

Both 2D and 3D Navier-Stokes computations will be performed. The time-step is set equal to $\Delta t = 2\times10^{-2}$ for both cases, and the meshes used are the sames as used so far. The 2D computation will be performed with the $k-\omega$ SST turbulence model, whereas the 3D simulations will be performed both with the $k-\omega$ SST and the DES model.

6.2 Analysis of the Results

2D $k-\omega$ SST and 3D DES Computations

Characteristic Loops

Figs.22 and 23 present the characteristic loops for lift and drag as a function of the angle of attack obtained with 2D $k-\omega$ SST and 3D DES computations respectively, and the experimental results. The curves with cross-points are the polar characteristics for the static airfoil obtained with the 2D $k-\omega$ SST Navier-Stokes code and the measurements. The experimental and 3D Navier-Stokes loops are averaged over several periods of the periodic pitching motion, as well as spanwise as for the Navier-Stokes computation. As for the 2D simulation, it was found that the flowfield became rapidly periodic after a short transient period of time, therefore the corresponding characteristic loops do not need to be averaged in this case.

An important characteristic of the loops, which is not obvious on the figures and needs to be emphasised, is the direction in which the loops are oriented during a time period of the pitching motion. All lift loops are actually oriented clockwise. As for the drag, it was found that both the experimental and 3D computed loops were oriented clockwise, whereas the 2D computed loop was oriented reversely. However, the opening of the 3D loop is quite small.

Compared to the experimental results, it can be seen that the 2D results overpredict the lift, especially at the end of the upward motion of the airfoil, and underestimate the drag (Fig.22). This is coherent with the static polar characteristics also shown on the figures. Wiggles due to the vortex shedding can be observed at the beginning of the downward phase of the periodic pitching motion.

The 3D computation slightly underpredicts both the lift and the drag. However, the opening, the shape and the slope of the loops obtained with the 3D computation are quite close to the experimental results (Fig.23).

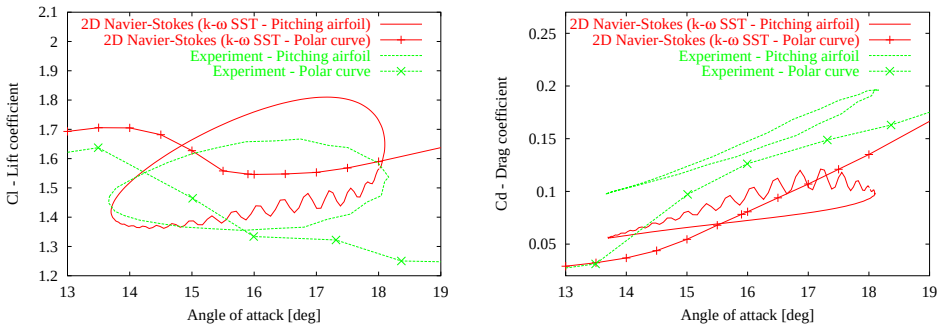

(a) Lift (b) Drag

Figure 22. Characteristic Loops for Pitching Airfoil ($\alpha = 15.9 \pm 2.2^o$)

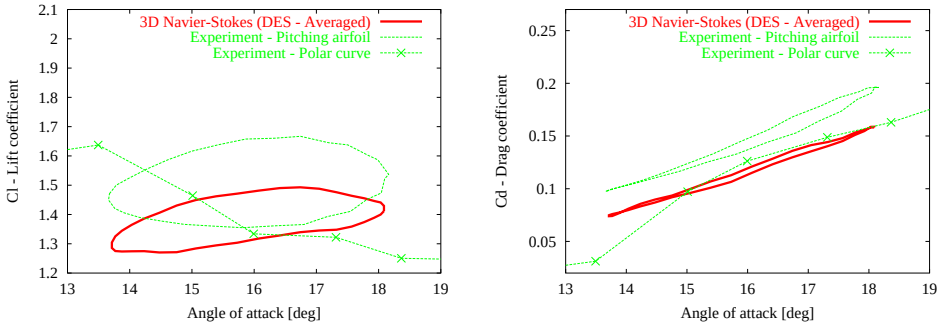

(a) Lift (b) Drag

Figure 23. Characteristic Loops for Pitching Airfoil ($\alpha = 15.9 \pm 2.2^o$)

The non-averaged characteristic loops are plotted on Fig.24 for the 3D DES Navier-Stokes computation (Note that the lift and drag have been averaged along the airfoil span in this case), and on Fig.25 for the experimental data. By comparing these figures, it can be seen that the experimental results exhibit a much more spread cloud of data.

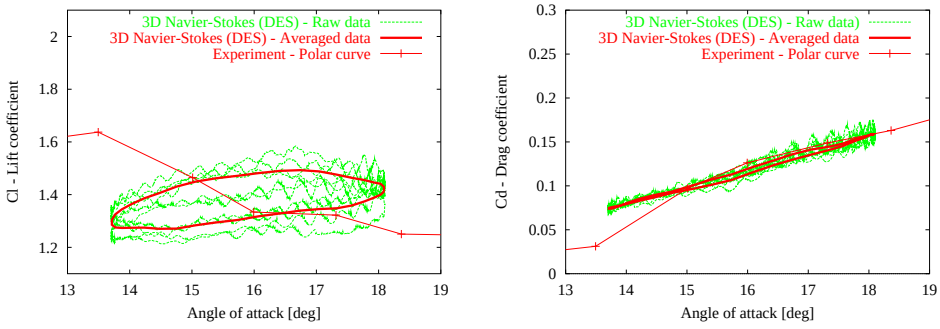

(a) Lift (b) Drag

Figure 24. Characteristic Loops for Pitching Airfoil ($\alpha = 15.9 \pm 2.2^o$) - DES

Time-Series

The time-series of lift and drag for the 2D $k-\omega$ SST and 3D DES computations are

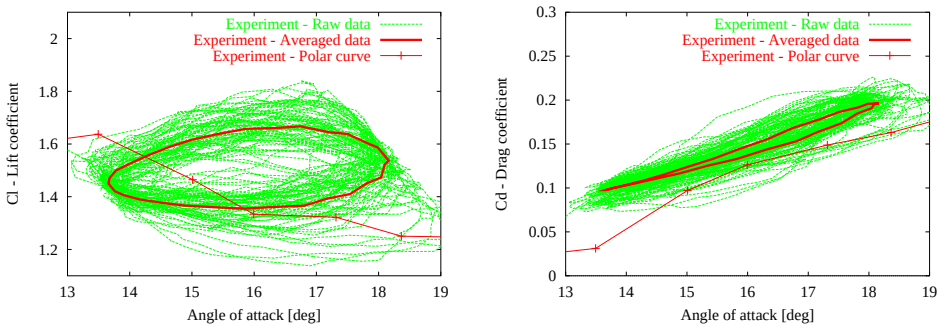

(a) Lift (b) Drag

Figure 25. Characteristics Loops for Pitching Airfoil ($\alpha = 15.9 \pm 2.2^o$) - Experiment

plotted on Fig.26. As expected, the 2D computation exhibits a periodic behavior whereas the 3D computation is not purely periodic.

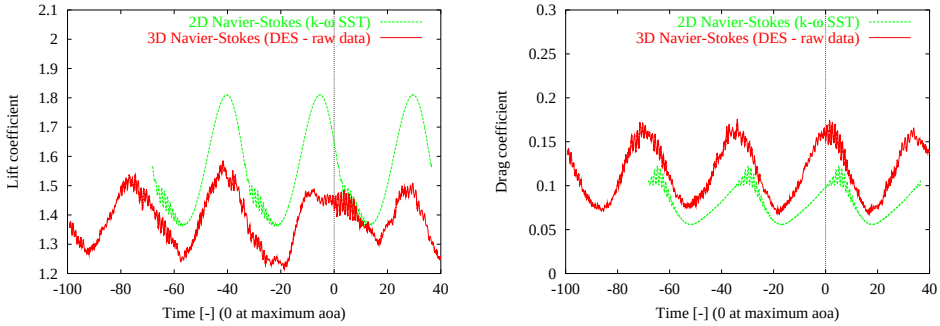

(a) Lift (b) Drag

Figure 26. Time-Series of Lift and Drag for Pitching Airfoil ($\alpha = 15.9 \pm 2.2^o$)

Pressure Coefficient Distributions

The next set of figures displays the pressure coefficient distributions on the profile at several specified angles of attack during one period of the pitching motion. The phase for which the angle of attack is increasing, or upward phase, is distinguished from the downward phase when the angle of attack is decreasing. Figs.27(a-e) display pressure coefficient for 2D $k-\omega$ SST and 3D DES computations, as well as experimental results, during the downward phase, and Figs.28(a-f) during the upward phase. As for the 3D computation, the pressure is averaged over the whole span of the blade (at a specific time), while the experimental results are averaged over several periods of the pitching motion. The pressure distributions are in relative good agreement during the downward phase, as observed in the lift loops (Figs.22(a) and 23(a)), but noticeably deviate from each other during the upward phase.

Figs.29 and 30 show the pressure coefficient distributions for the 3D DES computation at different locations along the span of the blade, together with the same 3D results averaged over the airfoil span and the averaged experimental results. It can be seen that the variation of the computed data in the spanwise direction is particularly large during the upward phase of the pitching motion, whereas the flow tends to be more two-dimensional during the downward phase.

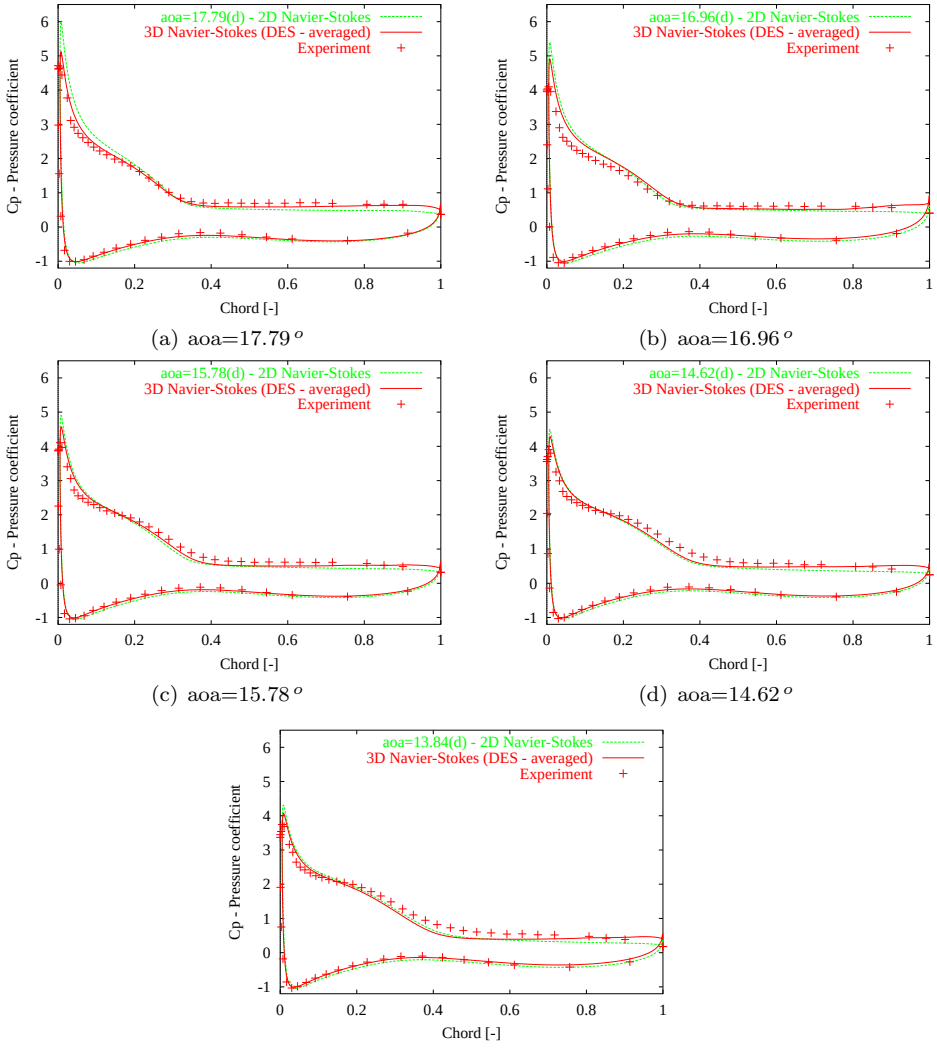

(a) aoa=17.79 ^{o} (b) aoa=16.96 ^{o}

(c) aoa=15.78 ^{o} (d) aoa=14.62 ^{o}

(e) aoa=13.84 ^{o}

Figure 27. Pressure Coefficient in Downward AOA Phase of Pitching Airfoil ($\alpha = 15.9 \pm 2.2^o$)

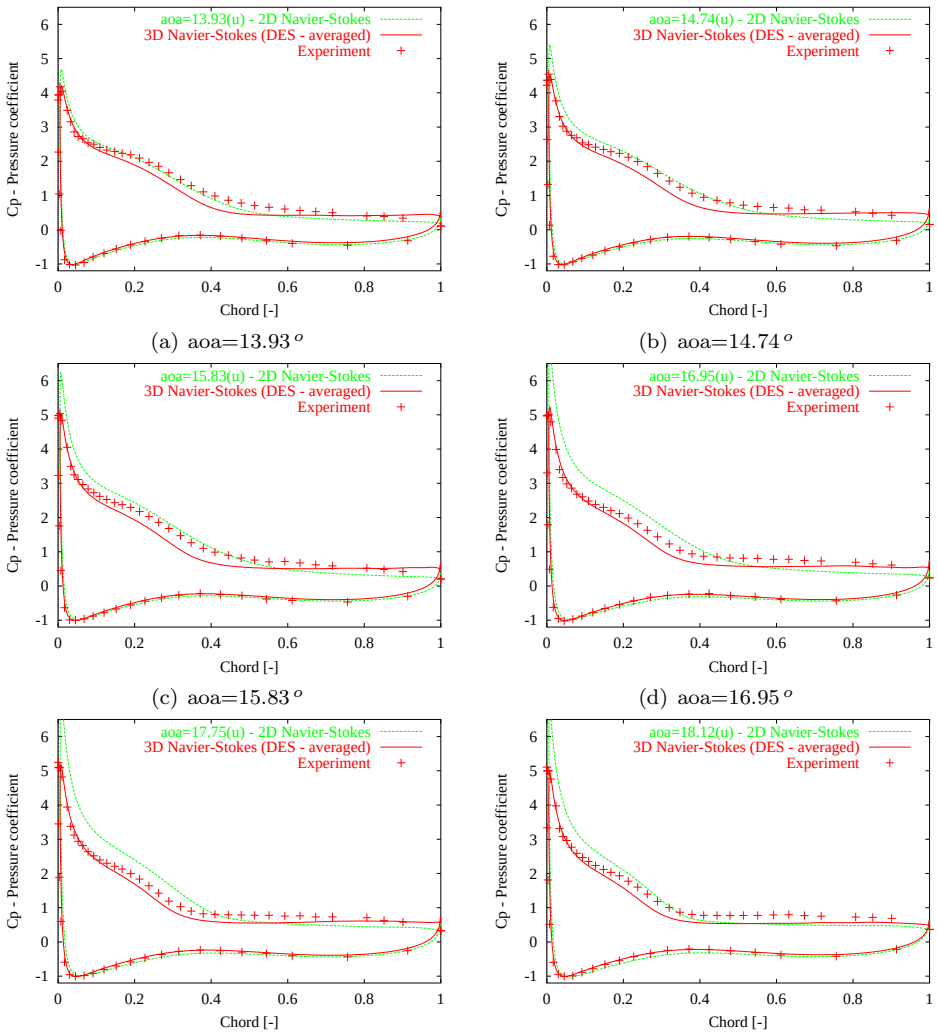

(a) aoa=13.93 ^{o} (b) aoa=14.74 ^{o}

(c) aoa=15.83 ^{o} (d) aoa=16.95 ^{o}

(e) aoa=17.75 ^{o} (f) aoa=18.12 ^{o}

Figure 28. Pressure Coefficient in Upward AOA Phase of Pitching Airfoil ($\alpha = 15.9 \pm 2.2^o$)

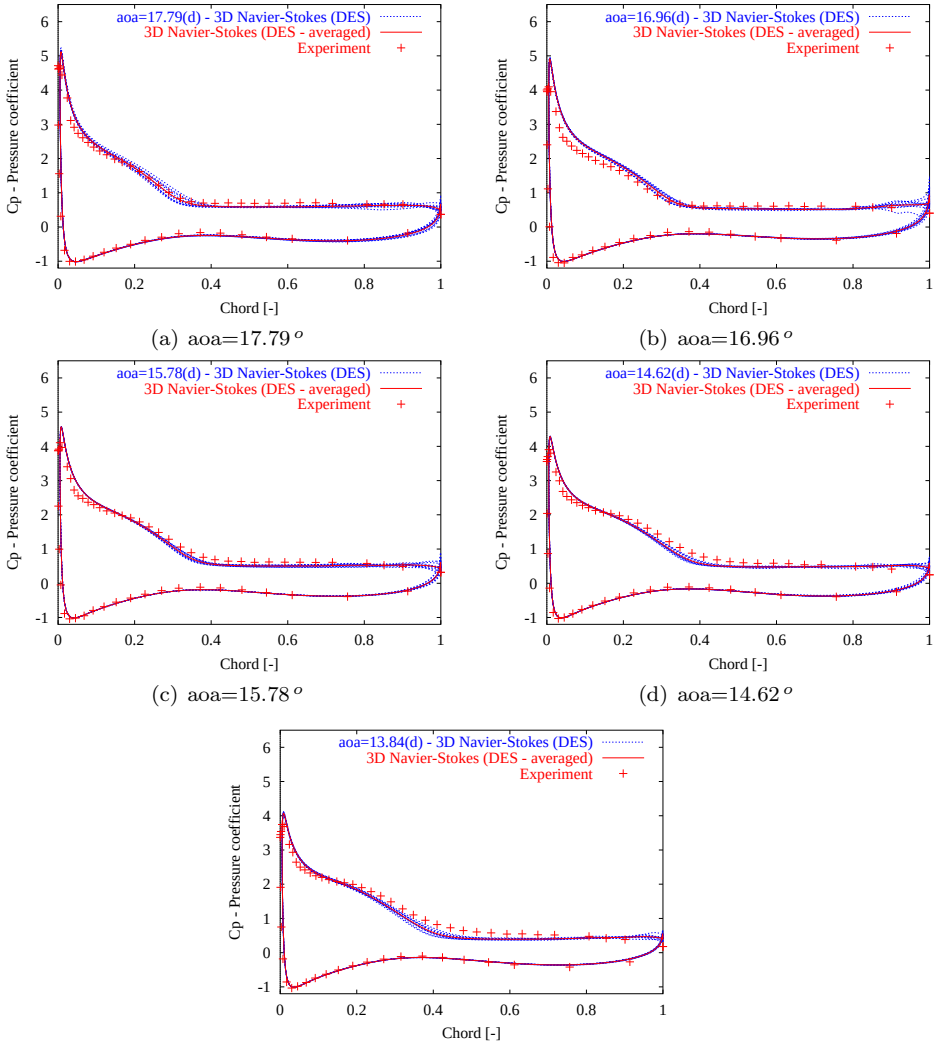

(a) aoa=17.79 ^{o} (b) aoa=16.96 ^{o}

(c) aoa=15.78 ^{o} (d) aoa=14.62 ^{o}

(e) aoa=13.84 ^{o}

Figure 29. Pressure Coefficient in Downward AOA Phase of Pitching Airfoil ($\alpha = 15.9 \pm 2.2^o$) - Spanwise Averaging

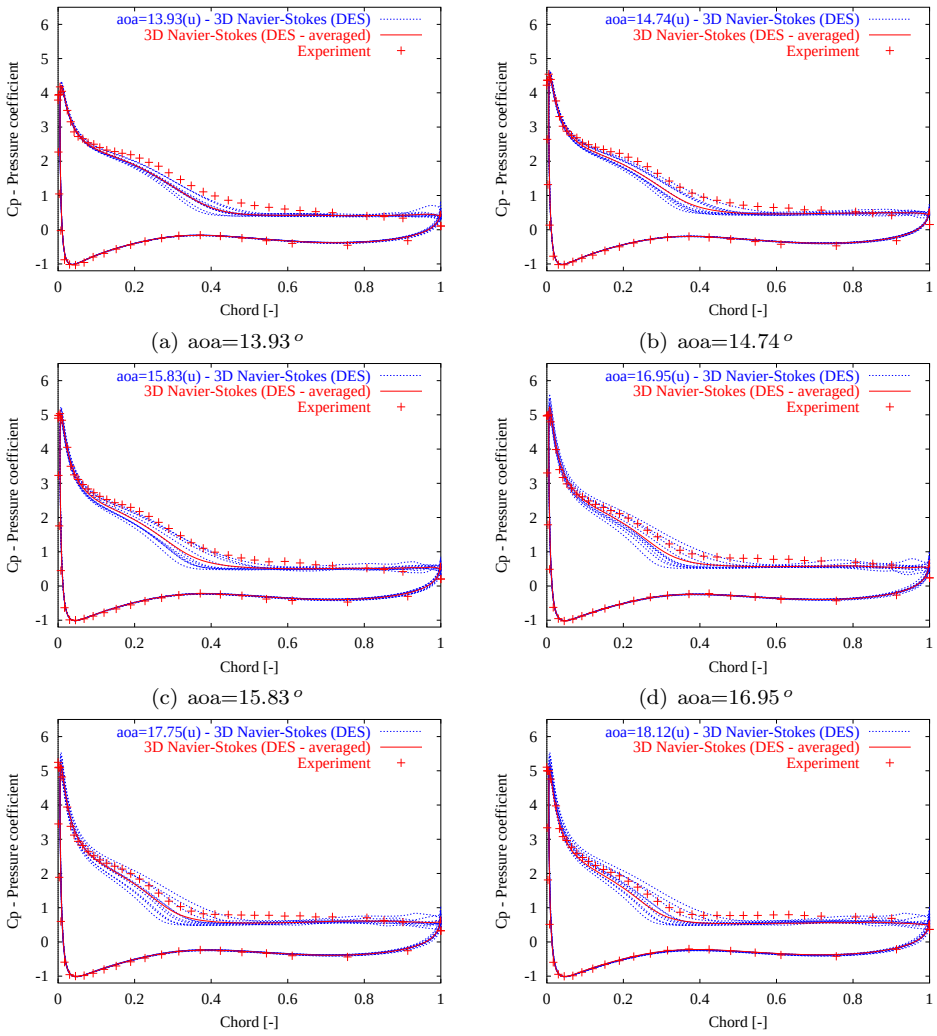

(a) aoa=13.93 ^{o} (b) aoa=14.74 ^{o}

(c) aoa=15.83 ^{o} (d) aoa=16.95 ^{o}

(e) aoa=17.75 ^{o} (f) aoa=18.12 ^{o}

Figure 30. Pressure Coefficient in Upward AOA Phase of Pitching Airfoil ($\alpha = 15.9 \pm 2.2^o$) *- Spanwise averaging*

Spanwise Slices

The time-series of the lift and drag of the 3D DES computation are presented on Figs.31(a-b) at several sections across the blade, as well as the corresponding values averaged across the blade span. The influence of the periodic pitching motion can clearly be seen on these time-series. A FFT analysis of these signals (Figs.33) reveals that the same flow patterns are present on all sections. In the low frequency range, the periodic motion which has a non-dimensionlised frequency of 0.033 can be observed. In the higher frequency range, the two-dimensional vortex shedding which was already present in the static computation (see previous section) can be observed at a frequency approximately equal to 1.

Short time extracts of the time-series are displayed on Figs.32(a-b). Even if the sampling frequency for the drag and lift at the slice sections is not very refined, it can clearly be seen that the vortex shedding, characterized by wiggles of a period approximately equal to 1, is well correlated between the different slices. This confirms that the vortex shedding is a 2D pattern that takes place on the whole span of the airfoil.

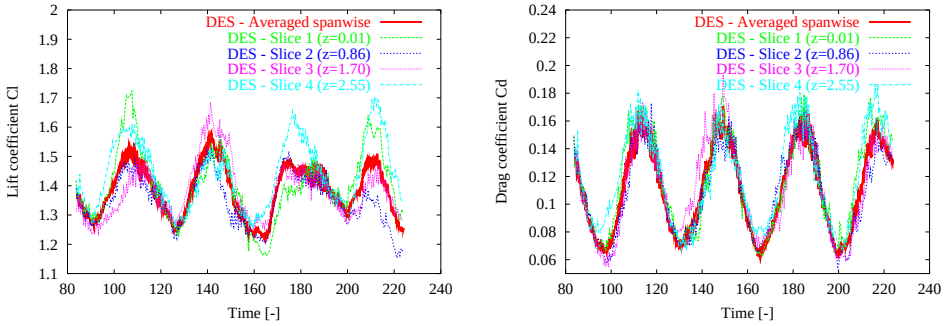

(a) Lift (b) Drag

Figure 31. Time-Series of Lift and Drag Spanwise along Pitching Airfoil ($\alpha = 15.9 \pm 2.2^o$)

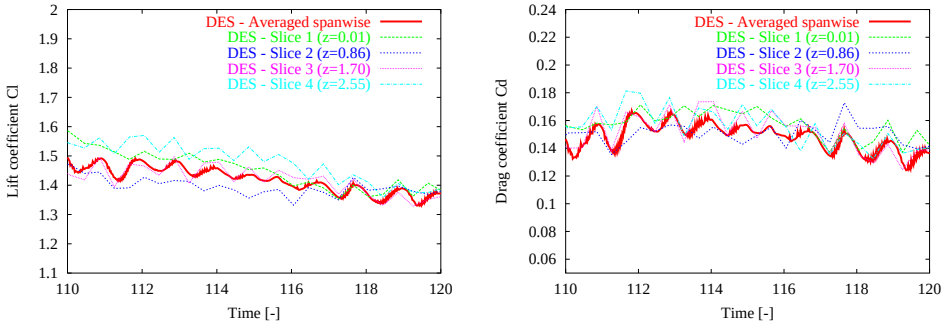

(a) Lift (b) Drag

Figure 32. Time-Series of Lift and Drag Spanwise along Pitching Airfoil ($\alpha = 15.9 \pm 2.2^o$) - Short Time Extract

Power Spectrum of the Signals

In Figs.34(a) and 35(a), FFTs of lift and drag, respectively, are plotted for the spanwise averaged results of the 3D DES computation, the 2D $k-\omega$ SST computation and the experimental results. Both 2D and 3D results exhibit a peak around a frequency of 1 corresponding to the two-dimensional vortex shedding pattern. Unfortunately, the sampling frequency of the experimental measurements is not high enough for capturing this pattern. It can be seen that this high frequency contribution is relatively small in term of spectral energy compared to the main pitching

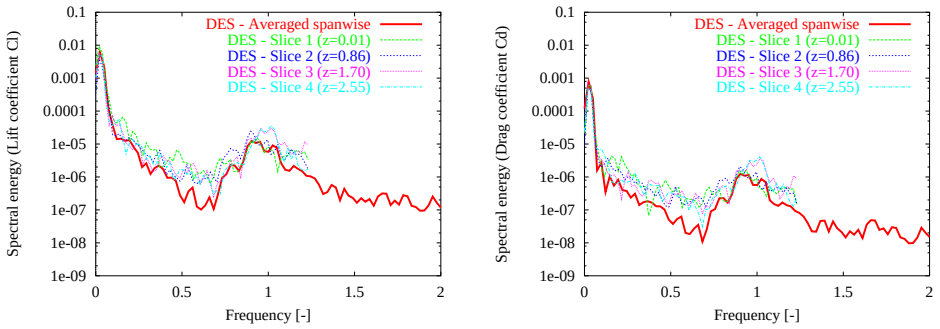

(a) Lift (b) Drag

Figure 33. Power Spectrum of Lift and Drag Spanwise along Pitching Airfoil ($\alpha = 15.9 \pm 2.2^o$)

motion energy peak. Indeed, the high frequency wiggles have a relatively small amplitude compared to the main oscillations of lift and drag due to the pitching motion (see Figs.31(a-b)). One may expect, that if this vortex shedding pattern exists in the experiment (as suggested in section 5.2), the variations induced by this phenomenon might be more significant, looking at the larger spreading of the raw experimental data observed in Fig.25.

Details of the power spectrum for the low frequencies is given on Figs.34(b) and 35(b). Computational results and experimental data exhibit high spectral power energy near the frequency of the pitching motion, though only the experimental data has enough data points to resolve this peak accurately.

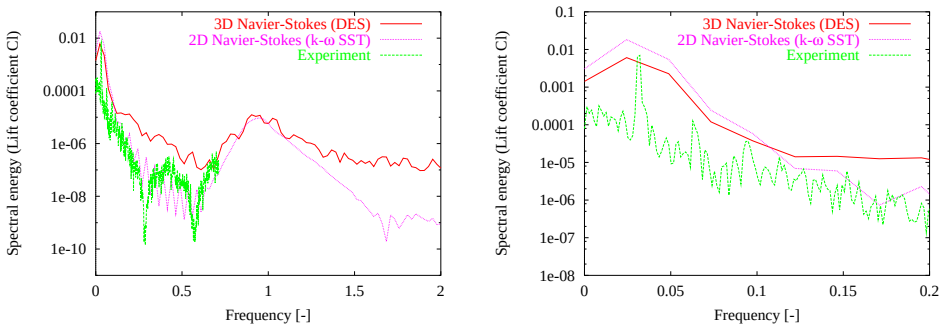

(a) Extended Spectrum (b) Detail of Low Frequencies

Figure 34. Power Spectrum of Lift for Pitching Airfoil ($\alpha = 15.9 \pm 2.2^o$)

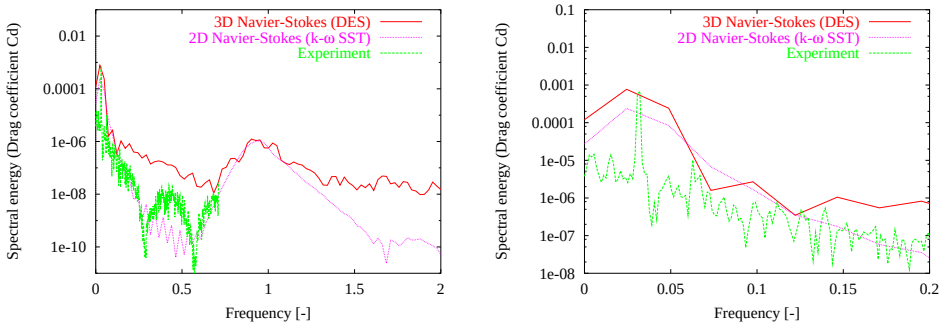

(a) Extended Spectrum (b) Detail of Low Frequencies

Figure 35. Power Spectrum of Drag for Pitching Airfoil ($\alpha = 15.9 \pm 2.2^o$)

3D $k-\omega$ SST Computation

The case of the pitching airfoil using the 3D $k-\omega$ SST turbulence model is now considered. Figs.36(a-b) show the lift and drag loops. Polar characteristics for the 2D $k-\omega$ SST model, as well as pitching loops for the 2D $k-\omega$ SST and the 3D DES results are also reported. It can be observed that the phenomenon observed in the case of the static airfoil at an angle of attack of 15.9^o also occurs in this case. Namely, the 3D $k-\omega$ SST model predicts lower lift and higher drag than the 2D $k-\omega$ SST model.

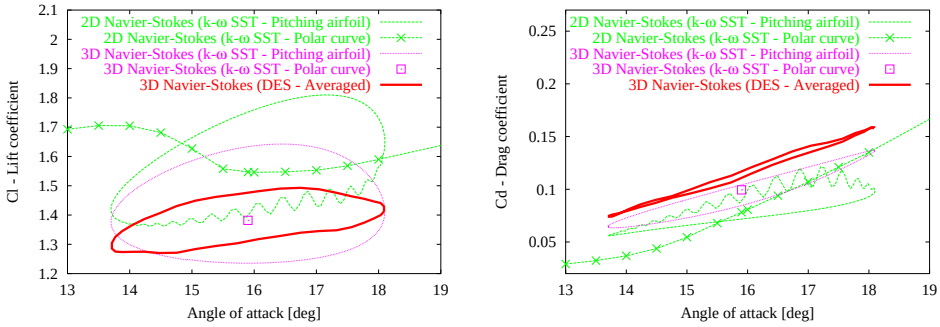

(a) Lift (b) Drag

Figure 36. Characteristic Loops for Pitching Airfoil ($\alpha = 15.9 \pm 2.2^o$)

Figs.37(a-b) display the lift and drag loops at several stations along the airfoil section. As it can be seen, the average level of the several loops is not constant along the airfoil span, indicating the presence of the same three-dimensional pattern already observed in the case of the static airfoil in the previous section (see section 5.2). Even if lift and drag evolve during the pitching motion, this three-dimensional structure remains stable in time. Moreover, the vortex shedding phenomenon observed for the 2D $k-\omega$ SST and 3D DES computations does not occur.

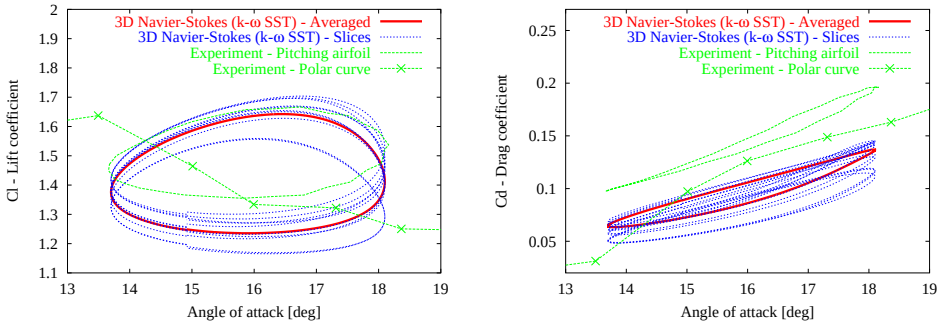

(a) Lift (b) Drag

Figure 37. Characteristic Loops along Pitching Airfoil ($\alpha = 15.9 \pm 2.2^o$)

Finally, the pressure coefficient distribution at several stations along the airfoil is compared with the 2D $k-\omega$ SST results on Figs.38 and 39. Again, it can be seen that the flow field is not similar along the airfoil due to the presence of the 3D structure for the 3D $k-\omega$ SST computation.

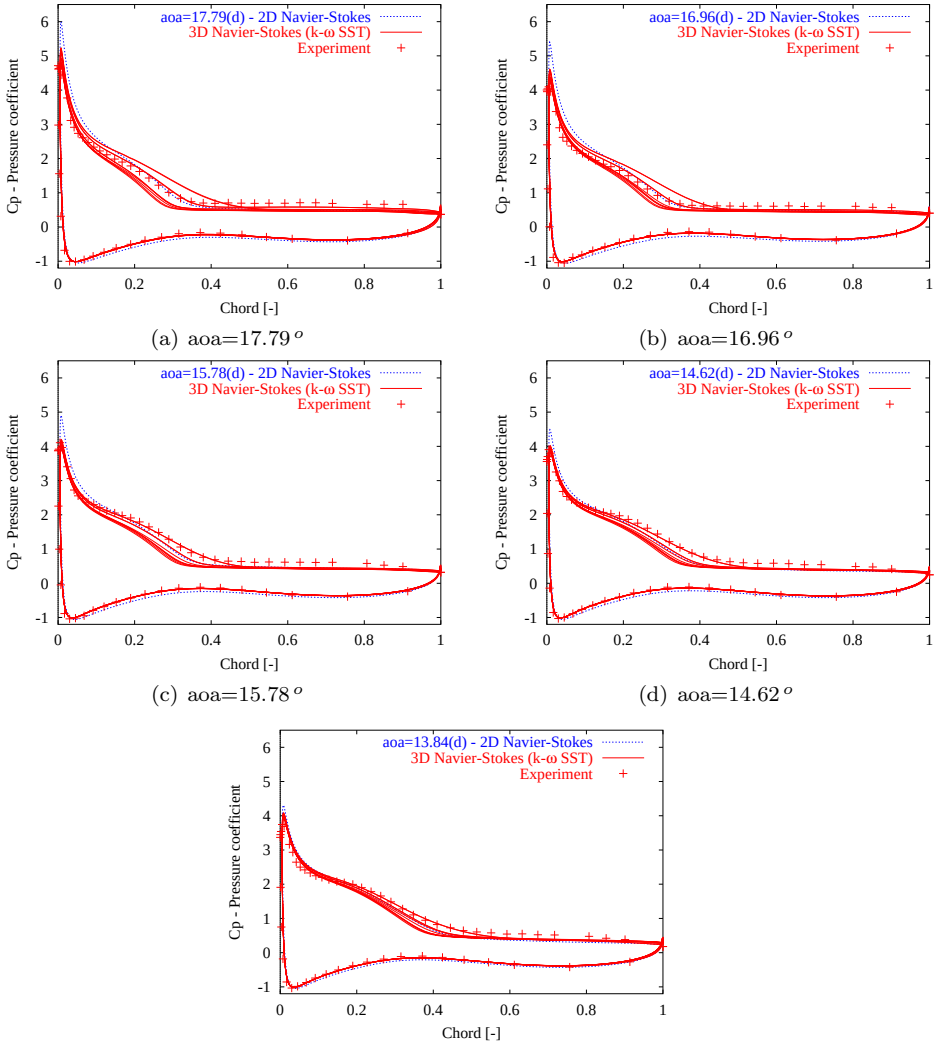

(a) aoa=17.79 ^{o} (b) aoa=16.96 ^{o}

(c) aoa=15.78 ^{o} (d) aoa=14.62 ^{o}

(e) aoa=13.84 ^{o}

Figure 38. Pressure Coefficient in Downward AOA Phase of Pitching Airfoil ($\alpha = 15.9 \pm 2.2^o$)

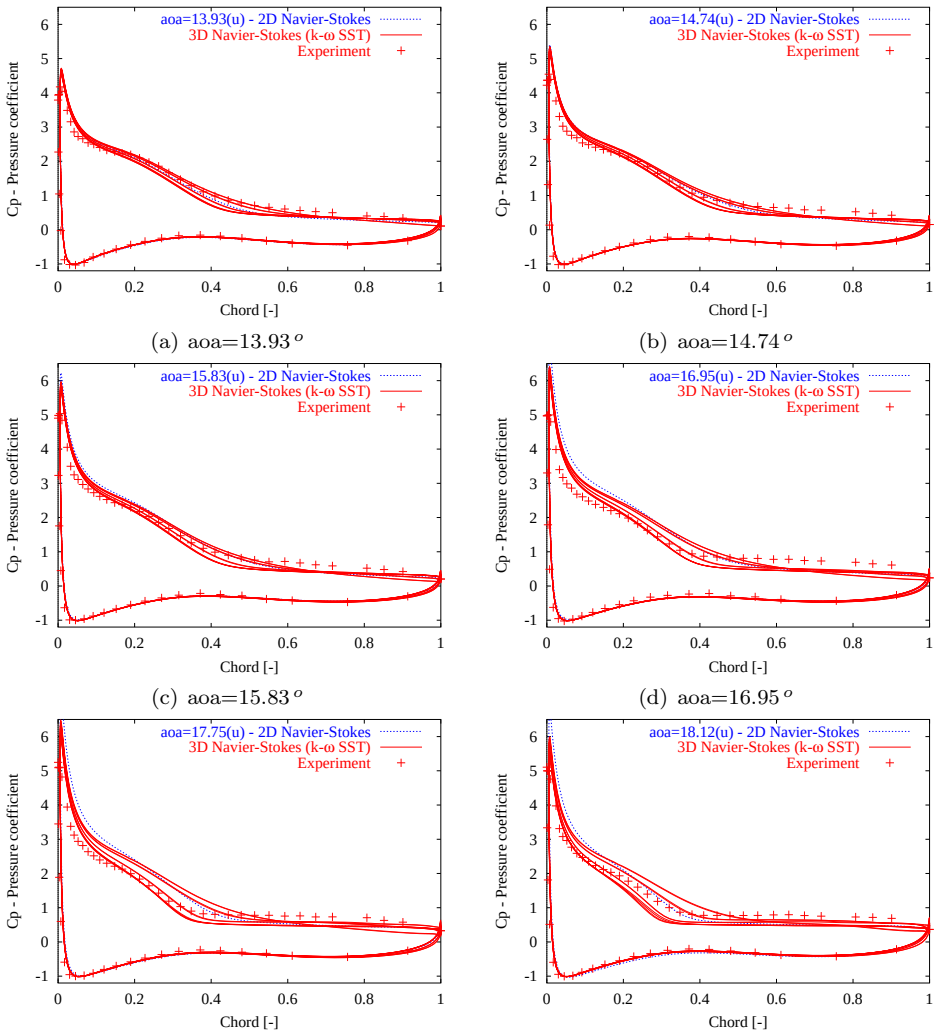

(a) aoa=13.93 ^{o} (b) aoa=14.74 ^{o}

(c) aoa=15.83 ^{o} (d) aoa=16.95 ^{o}

(e) aoa=17.75 ^{o} (f) aoa=18.12 ^{o}

Figure 39. Pressure Coefficient in Upward AOA Phase of Pitching Airfoil ($\alpha = 15.9 \pm 2.2^o$)

7 Semi-Empirical Dynamic Stall Model

This section is dedicated to the comparison of Navier-Stokes computations, experimental results and the semi-empirical dynamic stall model by Beddoes-Leishman [3]. The test case that is considered is the pitching motion of the RISØ-B1-18 airfoil as studied in the previous section [5]. In a second step, it will be tried to make benefit of these comparisons in order to improve the prediction capabilities of the dynamic stall model.

7.1 Comparison with the Dynamic Stall Model

Semi-empirical dynamic stall models require static polar characteristics as an input. In our case, two such sets of data are available: the experimental one and the one obtain with 2D computations as described in section 5. The two cases are reported on Figs.40(a-b). As expected, the two different loops are following the static polar characteristics on which they are based.

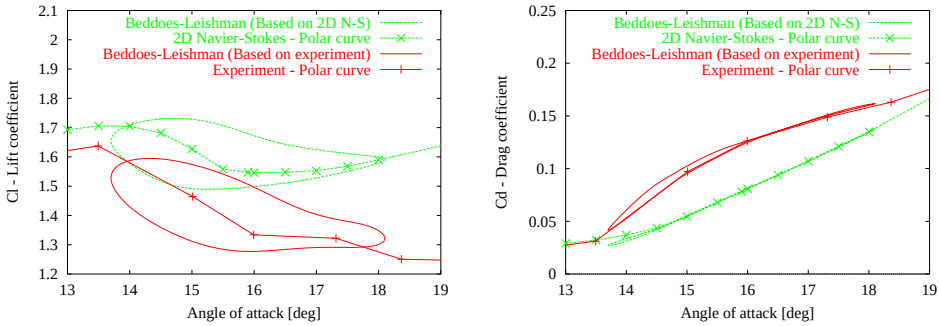

(a) Lift (b) Drag

Figure 40. Characteristic Loops for Pitching Airfoil ($\alpha = 15.9 \pm 2.2^o$) - Semi-empirical Models

In the next step, the time-series of lift and drag for the 2D $k-\omega$ SST and 3D DES Navier-Stokes computations, as well as experimental results, are compared to the Beddoes-Leishman model based on experimental polar characteristics on Figs.41(a-b). All curves are temporally synchronized such that at $t=0$, the angle of attack is maximum.

It can be seen that 2D and 3D Navier-Stokes computations have a relative good phase agreement with the experimental lift, even if the averaged value of lift and the amplitude of the variations are relatively different, as already observed in the previous section. The Beddoes-Leishman model exhibits quite a large phase delay and the signal seems to be advanced in time by approximately one third of the pitching period.

As for the drag, the situation is somehow different. Both the 3D Navier-Stokes computation and the Beddoes-Leishman model are in good phase agreement with the experimental data, whereas the 2D Navier-Stokes results exhibit a phase delay, particularly in the upward phase of the pitching motion, but this delay seems to disappear in the course of the downward phase.

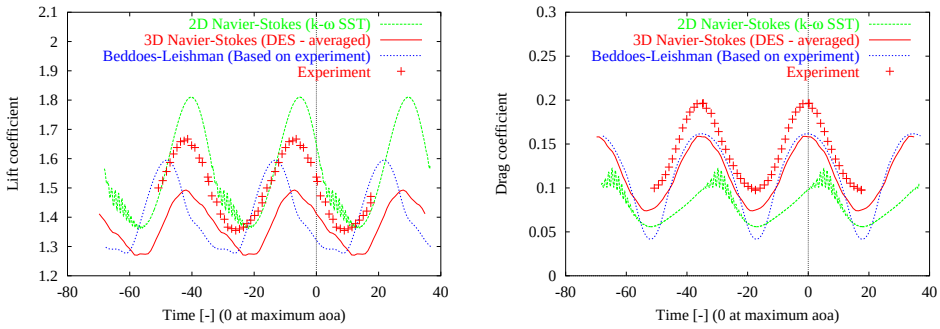

(a) Lift (b) Drag

Figure 41. Time-Series of Lift and Drag for Pitching Airfoil ($\alpha = 15.9 \pm 2.2^o$) - Semi-empirical Models

7.2 Tuning of the Dynamic Stall Model

In this section, all results obtained with the Beddoes-Leishman model are based on the experimental polar characteristics (see above).

In order to improve the results obtained with the Beddoes-Leishman model, the model parameter controlling the time-lag of boundary layer separation is tuned by increasing this parameter. The factor is denoted as τ_{BL} and was set originally to 3. Two other larger values are tested:

$$\tau_{\mathrm{BL}} = 12 \qquad \text{and} \qquad \tau_{\mathrm{BL}} = 24$$

The resulting time-series of lift and drag are presented on Figs.42(a-b), and the corresponding lift and drag loops on Figs.43(a-b). As it can be seen, the time delay in the time-series of lift that was observed decreases as the parameter τ_{BL} is increased (Fig.42(a)), whereas modifying the time-delay parameter has almost no influence on the drag time-dependency (Fig.42(b)).

It is thereby possible to obtain a characteristic lift loop which has a very similar opening and a very similar slope as the one obtained for the 3D computation with the DES model for the highest value $\tau_{\mathrm{BL}} = 24$, even though there still exists a small difference in the average lift level (see Fig.43(a)).

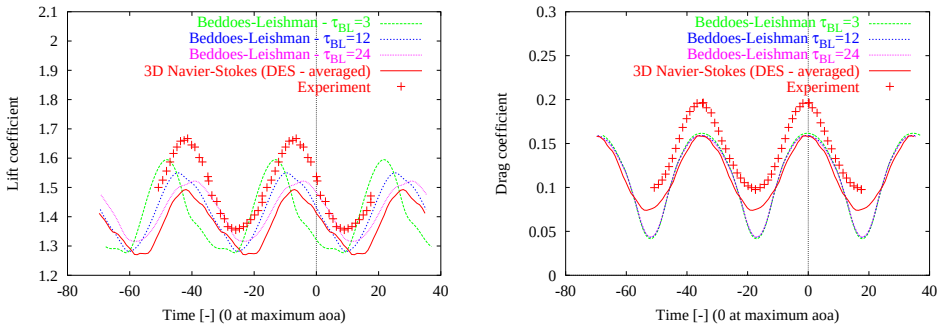

(a) Lift (b) Drag

Figure 42. Time-Series of Lift and Drag for Pitching Airfoil - Comparison of Semi-empirical Models

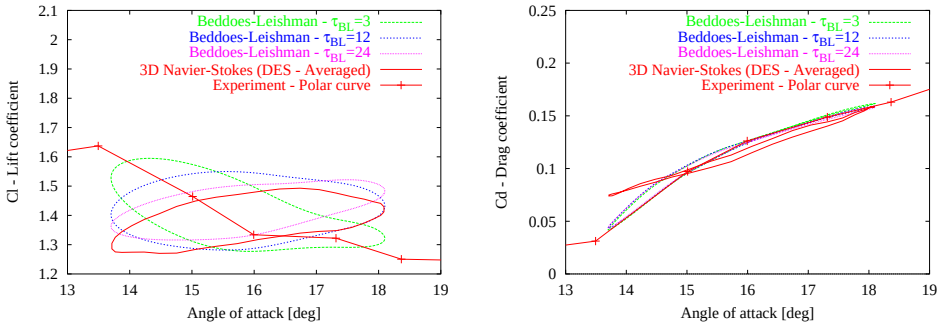

(a) Lift (b) Drag

Figure 43. Characteristic Loops for Pitching Airfoil - Comparison of Semi-empirical Models

8 Computation of Aerodynamic Damping

This section is dedicated to the comparison of Navier-Stokes computations, experimental results and the Beddoes-Leishman dynamic stall model in the case of the pitching RISØ-B1-18 airfoil as studied in the two previous sections [5]. However, the emphasis is now on the computation of the aerodynamic damping associated to the motion of the airfoil.

Note that the aerodynamic damping is directly proportional to the aerodynamic work performed by the fluid, up to a negative multiplicative constant depending on the geometry, the mass repartition in the airfoil section and the amplitude of the periodic deformation (see for example Clough and Penzien [21], or [22]). In this section, only the (opposite value of the) aerodynamic work will be plotted as we do not have access to a detailled description of the airfoil section geometry and the mass repartition.

As the airfoil is experiencing a periodic pitching motion, the aerodynamic damping can be computed by integrating the aerodynamic work performed by the fluid flow forces on the airfoil section during one period. In order to display continuous time-series, the aerodynamic work will actually be integrated over a 'sliding time-window' extending over one period of the periodic motion, and which boundaries follow the time evolution. At one time level, the computed aerodynamic work will then represent the work performed between that time level and the corresponding time level during the previous period.

Moreover, two ways of computing an aerodynamic work are derived. The first one, which is the actual aerodynamic work exerted on the airfoil, is obtained by time-integrating the product of the aerodynamic moment exerted by the fluid on the airfoil section and the angular velocity of the airfoil pitching motion. However, in a design process engineers are as well interested in the aerodynamic damping associated to a flapwise motion of the airfoil. Unfortunately such a configuration is not easy to implement in a wind tunnel, and therefore only a pitching motion of the airfoil could be achieved with the experimental devices that were available for the considered measurements [5]. Since we only do have access to experimental data for the pitching airfoil, an equivalent fictitious flapwise motion of the airfoil can be assumed, for which the angle of attack experienced during this imaginary plunging motion would be equal to the one actually experienced by the airfoil (during its pitching motion). Using the actual lift exerted on the airfoil section, it is then possible to compute an aerodynamic work associated to this imaginary flapwise motion. As it will be shown below, the assumption of this fictitious flapwise motion with an equivalent angle of attack is realistic as long as the amplitude of the pitching motion remains small. This methodology has proven to give coherent results with respect to an actual flapwise motion of the airfoil in the case of a 2D flow around a wind turbine airfoil in a previous numerical study [23].

8.1 Computing the Aerodynamic Work

As mentionned above, two ways of computing an aerodynamic work can be derived.

The first natural one is to time-integrate the work of the aerodynamic moment exerted on the airfoil section (per span unit length), and such during one period of the pitching motion:

$$W_{\text{pitching}}(t) = \int_{t-T}^{t} M(\tau)\,\dot{\alpha}(\tau)\;\mathrm{d}\tau$$

where α is the geometrical angle of attack of the airfoil as given in Eq.(1) in

section 6.1, t denotes the time, T is the period length of the pitching motion, and an upper dot denotes a time derivative. The period T is related to the angular velocity ω given in Eq.(2) by $\omega = 2\pi/T$. The aerodynamic moment M exerted by the fluid on the airfoil section (per unit length) is given as $M = C_m \times (\frac{1}{2}\rho V_\infty^2 C^2)$, where ρ is the fluid density, V_∞ the incoming velocity, C the airfoil chord, and C_m the dimensionless moment coefficient.

The second method for computing an aerodynamic work is described as follows. Let imagine that the airfoil is performing a flapwise motion perpendicular to the horizontal main flow velocity V_∞ as depicted in Fig.44, the airfoil having an angle of attack at rest equal to α_m (corresponding to the mean angle of attack of the previous pitching motion). We are looking for the vertical displacement of the airfoil $y(t)$ such that the resulting angle of attack that would be experienced by the airfoil in this flapwise motion equals the actual one of the pitching motion given as in Eq.(1):

$$\alpha(t) = \alpha_m + A\sin(\omega t) \tag{3}$$

where A is the amplitude of the pitching motion, and ω its angular velocity. The angle of attack relatively to the flow field experienced by the airfoil during its fictitious flapwise motion would be equal to:

$$\alpha(t) = \alpha_m - \widetilde{\alpha}(t)$$

where the variation of angle of attack $\widetilde{\alpha}$ is given as (see Fig.44):

$$\tan(\widetilde{\alpha}(t)) = \frac{\dot{y}(t)}{V_\infty} \tag{4}$$

Assuming that $\widetilde{\alpha}$ remains small (which is quite justified in our case as we are interested in a pitching motion for which the amplitude of the angle of attack variation is given as $A = 2.2^o$), then Eq.(4) can be approximated as:

$$\widetilde{\alpha}(t) \approx \frac{\dot{y}(t)}{V_\infty}$$

Combining the previous equations and integrating the resulting flapwise velocity yields:

$$y(t) = \frac{A\,V_\infty}{\omega}\cos(\omega t) + c \tag{5}$$

where the integration constant c can be set to 0 without loss of generality. The fictitious work (per span unit length) associated to this imaginary flapwise motion can then be computed as:

$$W_{\text{flap}}(t) = \int_{t-T}^{t} F_y(\tau)\,\dot{y}(\tau)\;\mathrm{d}\tau$$

where the aerodynamic force (per unit length) exerted by the fluid in the flap direction is given as $F_y = C_l \times (\frac{1}{2}\rho V_\infty^2 C)$, C_l being the lift coefficient.

8.2 Assessment of the Equivalence Pitching/Plunging Motions

To assess that the above described methodology is consistent, two computations are performed with the Beddoes-Leishman model. The first one is a pitching motion of the airfoil according to the angle of attack given by Eq.(3), the second one is a plunging motion for which the vertical displacement is given by Eq.(5). Fig.45(a) displays the time history of the angle of attack experienced by the airfoil in both cases. As it can be seen, there is a very good agreement confirming that the approximation made above is justified.

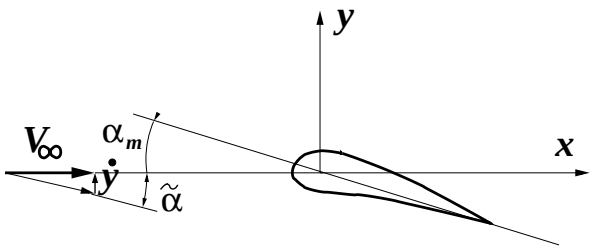

Figure 44. Description of the Flapwise Motion of the Airfoil

Lift, drag and moment loops as a function of the angle of attack are displayed on Figs.45(b-c-d), respectively. There is a quite good agreement between the lift and drag loops for the two methodologies. However, there exists some discrepancies for the moment coefficient loops. This is due to the fact that pitching and plunging motions lead to different dynamics of the moment exerted on the airfoil, when the lift time history is mostly driven by the angle of attack evolution which is almost identical in the two kinds of motion.

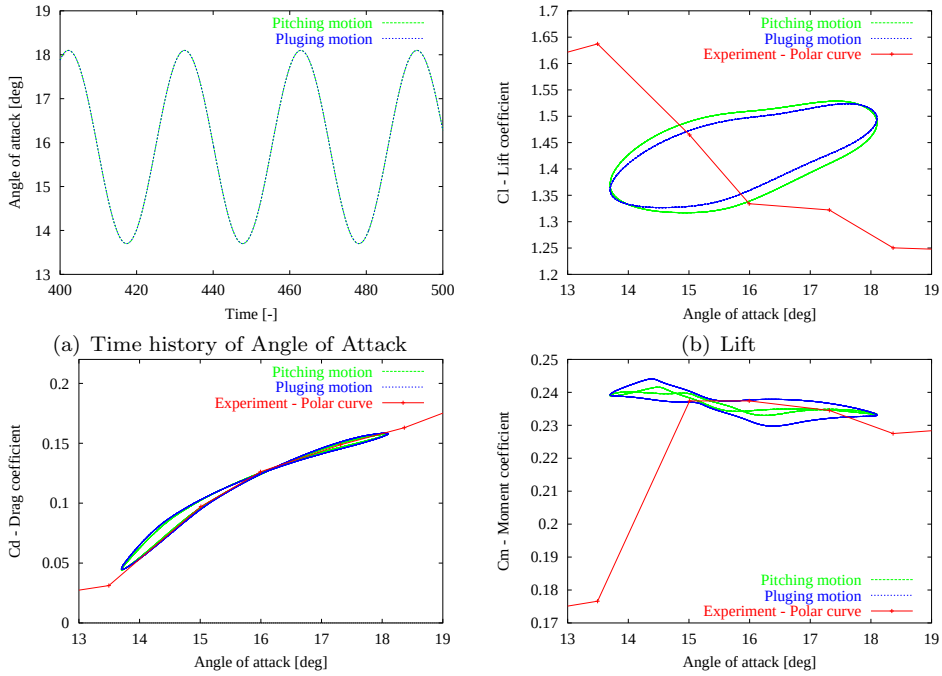

(a) Time history of Angle of Attack

(b) Lift

(c) Drag

(d) Moment

Figure 45. Comparison of the Pitching and Plunging Motions

8.3 Comparison of the Results

The aerodynamic works computed with the 3D Navier-Stokes DES computation, experimental data and the Beddoes-Leishman model ($\tau_{\mathrm{BL}} = 24$, see section 7.2) are compared on Fig.46(a) for the pitching motion, and on Fig.46(b) for the equivalent fictitious plunging motion.

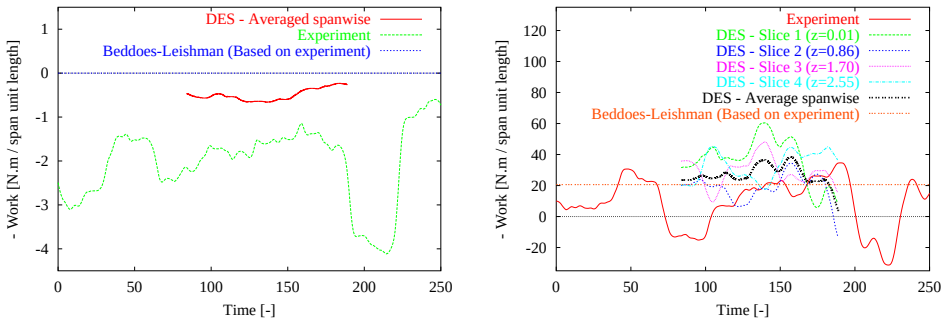

(a) Work based on C_m (b) Work based on C_l

Figure 46. Aerodynamic Work Computed on a Sliding Window - Comparison of Different Models

As it can be seen, the work computed by considering the actual pitching motion or for the equivalent plunging motion are of opposite sign, and of different orders of magnitude. This does not mean that there exits an inconsistency in the two ways of computing the aerodynamic work. It just illustrates the fact that the works computed by this two processes involve different features of the aerodynamic forces. Indeed, there is a priori no time-correlation between the aerodynamic lift and moment exerted on the airfoil (even though the pitching and the fictitious plunging motions are correlated through Eqs.(3) and (5)).

It can be noted on Fig.46(a) that the aerodynamic work computed for the Beddoes-Leishman model and based on the pitching motion is very small compared to the Navier-Stokes computation and the experimental results. It is due to the fact that in our implementation of the Beddoes-Leishman model, the pitching moment describes an almost closed loop (as a function of the angle of attack) as observed on Fig.45(d), resulting in a small contribution to the aerodynamic work.

It must be noted that the Beddoes-Leishman model always predicts a constant work on the sliding window as the computed aerodynamic lift and moment are purely periodic. Conversely, it can be seen that the Navier-Stokes DES computation and the experimental measurements predict an aerodynamic work that varies quite noticeably in time. It can even change sign sometimes as illustrated on Fig.46(b) for the experimental results. Indeed, most of the time the experimental aerodynamic lift leads to a positive damping of the plunging motion, but during extents of time (which can last as long as a period of the periodic motion $T \approx 34.9$ [-]) the aerodynamics implies a negative damping of the plunging motion (Remind that on Fig.46, the opposite of the aerodynamic work is plotted, which is then proportional to the damping). The Navier-Stokes computation seems to predict similar results, unfortunately the computation was not run long enough to observe if the damping would remain negative for a long extent of time (see Fig.46(b)).

9 Conclusions

The results obtained in the first part of this study proved that the 2D Navier-Stokes code with a RANS approach (using the $k-\omega$ SST turbulence model) was accurate enough to predict the lift and drag for the considered airfoil as long as the flowfield remains attached, both in the case of the static and the pitching airfoil. Above stall, the results deteriorates and one has to resort to more accurate turbulence modelling, at least in the case of a pitching airfoil.

The 3D computations with DES model gave good results both for a static and the pitching airfoil. However, in the static case the numerical model proved to predict stall slightly earlier than in the experiment. The 3D RANS simulation also proved to perform well in the case of a static airfoil, even after stall. In this latter case, the flowfield proved to remain steady but exhibited a 3D pattern. The question whether the presence of a similar 3D pattern is responsible for the good predictions of the 3D DES model (but couldn't be observed due to the chaotic nature of the flowfield), rather than the intrinsic unsteady flow features of the DES simulations, is still unanswered but could be a possible explanation. The same 3D pattern was also observed in the case of the pitching airfoil for the 3D RANS simulation. It proved to remain stable in time and was not destabilized by the pitching motion.

The presence of a trailing edge vortex shedding was observed both in the 2D unsteady RANS and the 3D DES computations. It remains unclear if it is present in the experiment, even though high frequency sampling measurements suggest that it does.

It was shown that it was possible to tune the semi-empirical model. However, it is difficult to say if this tuning will remain universal for different types of airfoil.

Finally, the aerodynamic work exerted on the pitching airfoil was calculated from the numerical computations (3D DES Navier-Stokes and Beddoes-Leishman model) and experimental results. By defining an equivalent fictitious plunging motion of the airfoil, it was shown that a periodic flapwise motion of the considered airfoil can become unstable both in the Navier-Stokes computation and in the experiment, the Beddoes-Leishman model being only able to predict a constant (and positive) aerodynamic damping.

Acknowledgements

This work was carried out under a contract with The Danish Energy Agency, ENS 1363/01-0001, Program for research in aeroelasticity 2001-2002. Computations were made possible by the use of the IBM RS/6000 SP at the Risø central computing facility, and the Danish Center for Scientific Computing in Aarhus.

References

[1] Bertagnolio, F., Gaunaa, M., Hansen, M.H., Sørensen, N.N. and Rasmussen, F., 2003,"Computation of Aerodynamic Damping Using CFD", 2003 ASME Wind Energy Symposium, at the 41st AIAA Aerospace Sciences Meeting and Exhibit, AIAA Paper 2003-0521, Reno, NV.

[2] Bertagnolio, F., Sørensen, N.N., Hansen, M.H. and Gaunaa, M., 2003,"Aeroelastic Simulation of a Wind Turbine Airfoil by Coupling CFD and a Beam Element Method", 2003 European Wind Energy Conference and Exhibition, Madrid, Spain.

[3] Leishman, J.G. and Beddoes, T.S., 1989, "A Semi-Empirical Model for Dynamic Stall", Journal of the American Helicopter Society, Vol.34, No.3, July 1989, pp.3-17.

[4] Fuglsang, P., Antoniou, I., Sørensen, N.N. and Madsen, H.Aa., 1998, "Validation of a Wind Tunnel Testing Facility for Blade Surface Pressure Measurements", Tech. Report Risø-R-981(EN), Risø National Laboratory, Roskilde, Denmark.

[5] Fuglsang, P., Bak, C., Gaunaa, M. and Antoniou, I., 2003, "Wind Tunnel Tests of Risø-B1-18 and Risø-B1-24", Tech. Report Risø-R-1375(EN), Risø National Laboratory, Roskilde, Denmark.

[6] Menter, F.R., 1993, "Zonal Two-Equations $k-\omega$ Turbulence Models for Aerodynamic Flows", AIAA Paper 93-2906.

[7] Simms, D., Schreck, S., Hand, M. and Fingersh, L.J., 2001, "NREL Unsteady Aerodynamics Experiment in the NASA-Ames Wind Tunnel: A Comparison of the Predictions to Measurements", Report NREL/TP-500-29494, National Renewable Energy Laboratory, Golden, CO.

[8] Fingersh, L., Simms, D., Hand, M., Jager, D., Cortrell, J., Robinson, M., Schreck, S. and Larwood, S., 2001, "Wind Tunnel Testing of NREL's Unsteady Aerodynamics Experiment", AIAA Paper 2001-0035, Reno, NV.

[9] Johansen, J., Sørensen, N.N., Michelsen, J.A. and Schreck, S., 2001, "Detached-Eddy Simulation of Flow around the S809 Airfoil", European Wind Energy Conference 2001, 2-6 July, Copenhagen, Denmark.

[10] Spalart, P.R., Jou, W-H., Strelets, M. and Allmaras, S.R., 1997, "Comments on the Feasibility of LES for Wings, and on a Hybrid RANS/LES Approach", Proc. of 1st AFOSR Int. Conf. on DNS/LES, Ruston, LA, August 4-8, Greyden Press, Columbus, OH.

[11] Michelsen, J.A., 1992, "Basis3D - A Platform for Development of Multiblock PDE Solvers", Tech. Report AFM 92-05, Technical University of Denmark, Lyngby, Denmark.

[12] Michelsen, J.A., 1994, "Block Structured Multigrid Solution of 2D and 3D Elliptic PDE's", Tech. Report AFM 94-06, Technical University of Denmark, Lyngby, Denmark.

[13] Sørensen, N.N., 1995, "General Purpose Flow Solver Applied to Flow over Hills", PhD Thesis, Tech. Report Risø-R-827(EN), Risø National Laboratory, Roskilde, Denmark.

[14] Rhie, C.M. and Chow, W.L., 1983, "Numerical Study of the Turbulent Flow Past an Airfoil with Trailing Edge Separation", AIAA Journal, Vol.21, pp.1525-1532.

[15] Issa, R.I., 1985, "Solution of the Implicitly Discretized Fluid Flow Equations by Operator-Splitting", J. Computational Physics, Vol.62, pp.40-65.

[16] Yeo, R.W., Wood, P.E. and Hrymak, A.N., 1991, "A Numerical Study of Laminar 90-degree Bend Duct Flow with Different Discretization Schemes", J. Fluids Eng., Vol.113, pp.563-568.

[17] Strelets, M., 2001, "Detached Eddy Simulation of Massively Separated Flows", 39th AIAA Aerospace Sciences Meeting and Exhibit, AIAA Paper 2001-0879, Reno, NV.

[18] Smagorinsky, J., 1963, "General Circulation Experiments with the Primitive Equations. I: The Basic Experiment", Month. Weath. Rev., Vol.91, No.3, pp.99-165.

[19] Hansen, M.H., Madsen, H.Aa. and Gaunaa, M., 2003, "A State-Space Formulation of the Beddoes-Leishman Dynamic Stall Model", Tech. Report Risø-R-1354(EN), Risø National Laboratory, Roskilde, Denmark.

[20] Bertagnolio, F., Sørensen, N.N. and Johansen, J., 2001, "Status for the Two-Dimensional Navier-Stokes Solver EllipSys2D", Tech. Report Risø-R-1282(EN), Risø National Laboratory, Roskilde, Denmark.

[21] Clough, R.W. and Penzien, J., 1975, Dynamics of Structures, Mc Graw Hill.

[22] Petersen, J.T., Madsen, H.Aa., Björck, A., Enevoldsen, P., Øye, S., Ganander, H. and Winkelaar, D., 1998, "Prediction of Dynamic Loads and Vibrations in Stall, Tech. Report Risø-R-1045(EN), Risø National Laboratory, Roskilde, Denmark.

[23] Bertagnolio, F. and Sørensen, N.N., 1997, "Numerical Simulation of the RISØ1-Airfoil Dynamic Stall", IEA Joint Action, Annex XI, Aerodynamics of Wind Turbines, 11th Symposium, ECN, Petten, Netherlands, 18-19 December.

Bibliographic Data Sheet **Risø–R–1448(EN)**

Title and author(s)

Numerical Study of the Static and Pitching RISØ-B1-18 Airfoil

Franck Bertagnolio

ISBN	ISSN
87–550–3298–2 (Internet)	0106–2840

Dept. or group	Date
Wind Energy Department	January 2004

Groups own reg. number(s)	Project/contract No.
1110401-00	ENS-1363/01-0001

Sponsorship

Danish Energy Authority

Pages	Tables	Illustrations	References
45	0	46	23

Abstract (Max. 2000 char.)

The objective of this report is the better understanding of the physics of the aeroelastic motion of wind turbine blades in order to improve the numerical models used for their design. In this study, the case of the RISØ-B1-18 airfoil which was equipped and measured in an open jet wind tunnel is studied. Two and three-dimensional Navier-Stokes calculations using the $k-\omega$ SST and Detached Eddy Simulation turbulence models are conducted. An engineering semi-empirical dynamic stall model is also used for performing calculations. Computational results are compared to the experimental results that are available both for the static airfoil and in the case of pitching motions. It is shown that the Navier-Stokes simulations can reproduced the main characteristic features of the flow. The DES model seems also to be able to reproduce some details of the unsteady aerodynamics. The Navier-Stokes computations can then be used to improve the performance of the engineering model.

Descriptors

AERODYNAMICS; AIRFOILS; COMPUTATIONAL FLUID DYNAMICS; TURBULENT FLOW; WIND TURBINES; WIND TUNNEL; VORTEX SHEDDING; STALL; AERODYNAMIC DAMPING; ENGINEERING MODEL

Available on request from:
Information Service Department, Risø National Laboratory
(Afdelingen for Informationsservice, Forskningscenter Risø)
P.O. Box 49, DK–4000 Roskilde, Denmark
Phone (+45) 46 77 46 77, ext. 4004/4005 · Fax (+45) 46 77 40 13
E-mail: risoe@risoe.dk